journal of the international meteor organization

WGN

48:2
april 2020

IMC 2020 in Poroszló, Hungary
Comet 15P/Finlay shower prediction for 2021
Three components of Taurids
Brief pre-maximum peak in Quadrantids 2020
Sporadic background from historic radar observations

ISSN 1016-3115

WGN Vol. 48, No. 2, April 2020, pp. 25 – 56

Conferences

Twenty-Ninth International Meteor Conference, Poroszló, Hungary, 2020 September 17–20 *Ákos Kereszturi* 25

Meteor science

Meteor shower output caused by comet 15P/Finlay *J. Vaubaillon, A. Egal, J. Desmars, K. Baillié* 29

Three components of 'Taurids' II *Masahiro Koseki* 36

A brief pre-maximum peak in the Quadrantids 2020 *Jürgen Rendtel, Hirofumi Sugimoto* 47

Radar meteors

Distribution of sporadic meteor background from 40-years old radar observations *Peter Zimnikoval, Daniel Očenáš, Miroslav Znášik, Juraj Škvarka, Ján Fabricius, Stanislav Kaniansky* 51

Front cover photo

Brilliant fireball shot through the aurora at $02^{h}08^{m}$ AKDT ($10^{h}08^{m}$ UT) on 2020 March 13, from Copper Center, Alaska, USA. Image courtesy: Todd Salat / `AuroraHunter.com`

Writing for WGN This Journal welcomes papers submitted for publication. All papers are reviewed for scientific content, and edited for English and style. Instructions for authors can be found in WGN **45:1**, 1–5, and at `http://www.imo.net/docs/writingforwgn.pdf` .

Legal address International Meteor Organization, Jozef Mattheessensstraat 60, 2540 Hove, Belgium.

Conferences

Twenty-Ninth International Meteor Conference, Poroszló, Hungary, 2020 September 17–20

Ákos Kereszturi[1]

1 Introduction

The conditions for the organization of the annual International Meteor Conference are unusual this year as the COVID-19 virus related restrictions currently inhibit the organization of large meetings. However, expectations show that the organization might be possible and officially allowed for the autumn. Thus the leaders of IMO and the Hungarian organizers progress with the preparations and hope the conditions will allow the meeting. This will be resolved in summer, thus all possible participants are requested to register, as without sufficient number of interested attendees the conference will not be held even if would have been officially allowed. Thus the organizers encourage you to register. In case if the meeting cannot be organized, full registration fees will be reimbursed for the registered persons.

Most of the scientific analysis based forecast of experts suggest that the virus and related uncomfortable situation will not disappear for about a year, and persons interested in international conferences could meet with each other if restrictions are kept carefully. The IMC 2020 provides all obligatory and recommended restrictions to keep a safe meeting. The conference site is accessible by cars from European countries without flight, all facilities support hygienic presence of attendees at this remote, countryside location.

2 Venue and location

The conference site is at the Great Hungarian Plain, Hortobágy area, nearby a village called Poroszló, about 140 km to the east of Budapest, 2 hours driving distance (Coordinates: 47.649976° N, 20.668603° E; Google maps link at `https://tinyurl.com/IMC2020-map`), at the lake called Tisza-tó, at the area of the Natural Reserve Hortobágy (part of the UNESCO World Heritage sites). The "Fűzfa Hotel és Pihenőpark" (Willow Hotel and Recreation Park, `https://fuzfapihenopark.hu/`) is a farm-like hotel, with buildings in 100–200 m walking distance from each other, except some of further rooms (especially single bed ones), which are in small motels around 20 minutes walking distance.

The site could host 120 persons (120 beds), 2/3 of them in a large house as separate rooms with 2, 3 and 4 beds. Further participants (especially those who require separate single rooms) will be accommodated in 10–20 min walking distance, and supported by a shuttle in the morning and evening. All rooms are equipped with private bathroom, fridge, air conditioning, and WIFI access. The 1/3 of the beds are located in small wooden houses, equipped also with private bathroom and fridge plus air conditioning system and WIFI access.

[1] Research Center for Astronomy and Earth Sciences. E-mail: `kereszturiakos@gmail.com`

Figure 1 – Location of the site on a map (left) and its aerial view (right).

The site includes thermal bath, sauna, indoor swimming pool and outdoor thermal bath, which could be used free of charge during the conference (Figure 3). There is a "night bar" where various drinks could be bought, three billiard tables can be used next to chairs and tables, around three bowling alleys (this last is not free of charge for use and the drinks in the bar are also should be payed for).

The weather at the end of September supposed to be mild with max. 20–25°C temperature daytime, 10–15°C nighttime and low probability of rain. Mosquitoes might be present, thus you might bring some spray against mosquitoes. In case if you require a visa, please contact the local organizers. The local currency of Hungary is forint – euro is not accepted. You need to convert your currency, which should be done in the main cities, however you may use your credit card.

3 Program and events

The scientific program will start in the evening of September 17 and will terminate at lunch September 20. The excursion of the IMC 2020 meeting will happen in the afternoon of September 19 (Saturday). The location

Figure 2 – Images of the main building (top left), one room interior (top right), some of the wooden houses (bottom left) and their interior (bottom right).

Figure 3 – The bowling alleys (left), the indoor swimming pool (middle) and the outdoor thermal bath (right).

is the natural reserve next to the meeting place, part of the Hortobágy National Park. The excursion will contain two parts, participants will be divided at least two groups, with alternating site visit, altogether for 2–3 hours:

1. The walking along the "water pathway" that follows of a 1.5 km long wooden plank system above the water, meandering in the reed system. The pathway crosses 3 small islands, 2 bird watching hides and a 15 m high scene watching tower. Information tables and guides will help you to get familiar with the unique plants and animals there.

2. The boat trip also takes you though the natural reserve, visiting such hidden locations that are not accessible during the walk. The natural environment is almost intact at the excursion site, thus please follow the directions and the rules explained by the guides, and consider the environment, keeping your trash with you and bring it back to the hotel.

4 Travel info

The conference site can be reached by 1.5 hour driving from Budapest. For persons arriving to the airport, a shuttle service will be provided for free. For ideal organization, please give your flight number and arriving / departing times at the registration site.

- Flight: to Budapest (BUD) Liszt Ferenc International Airport. From there the local organizers arrange 2 shuttle services around noon and late afternoon of the first day. There is a train access possibility from Budapest to Poroszló (see below) – however it is recommended to use the shuttle service provided by the

Figure 4 – The "water pathway" part of the excursion.

LOC for free from the airport (in case of arriving to one train or bus station in Budapest, please contact the organizers beforehand how to access the shuttle service starting point from there).

- Car: this is the ideal method to come to the site, what requires 2 hours driving from Budapest (mainly on the M3 highway that requires highway access ticket that costs 12 EUR). The travel time from some main cities by car are the followings: Bratislava 3.5 hours, Prague 7 hours, Berlin 12 hours.
- Train: from Keleti pályaudvar, i.e. the East railway station trains run around every 3 hours, the trip takes around 3 hours, but requires 3 changes (usually at Hatvan and Fuzesabony). For more information ask the LOC.

5 Registration and payment

The registration for the meeting is already opened at `https://imc2020.imo.net/registration`. The early bird registration fee is 180 EUR for standard accommodation in a double room for 3 nights (only) with full board + participation in the conference, conference materials, coffee breaks and excursion (price per person). There is a limited availability for single rooms (max. 10-15 min walking distance or if more, with shuttle for each day), what covers the accommodation in a single room for 3 nights (only) with full board + participation in the conference, conference materials, coffee breaks and excursion. There is a possibility to pay 100 EUR with no accommodation but with all meals except breakfasts + participation in the conference, conference materials, coffee breaks and excursion. Please register, and if there will be any cancellation because of the virus issue, all payment will be refunded. Members of the Local Organizing Committee are from the Konkoly Astronomical Institute (Research Centre for Astronomy and Earth Sciences) and the Hungarian Astronomical Nonprofit Ltd.

COVID-19 Info

We hope that the IMC 2020 in Hungary can take place as planned, on September 17–20, though this of course depends on the evolution of the COVID-19 pandemic and related policies.

We encourage people to register for the conference. The following guarantees may be of help:

1. In case the IMC 2020 is canceled due to COVID-19, all participants will get a total refund. The final decision will be taken on Friday, July 24 at the latest.
2. If travel between a participant's country and Hungary is not allowed at the time of the IMC, the participant will get a total refund.
3. Extended early bird registration deadline: July 15.
4. Registration deadline and presentation/poster deadline: August 31.

Meteor science

Meteor shower output caused by comet 15P/Finlay

J. Vaubaillon[1], A. Egal[2], J. Desmars[3], K. Baillié[4]

Theoretical work on the meteoroid stream ejected by comet 15P/Finlay predicts multiple outbursts in 2021 in agreement with previous authors. This work predicts the first outburst to happen around 2021-09-29T08:35 UT, for a radiant located at $\alpha = 260.^\circ 8$, $\delta = -57.^\circ 4$ and will be best visible from New-Zealand. The second will happen on 2021-10-07T00:35 UT, followed by a third on 2021-10-07T03:55 UT. They will be best visible from the tip of Antarctica or Tierra Del Fuego (Argentina). The level of each outburst is evaluated based on the photometry of the comet, which is known to have experienced some outbursts, but is less certain than the timing of each event.

Received 2019 December 20

1 Introduction

Meteor shower outburst are now commonly predicted (Vaubaillon et al., 2019). If the timing of occurrence of a meteor shower is pretty reliable, the level of an outburst is still today much harder and hazardous to assess. Recent success include the α-Monocerotids (Jenniskens & Lyytinen, 2019a; Jenniskens & Lyytinen, 2019b). The outburst was on time but the level was much less than expected. Though some observers might be disappointed, this also raises exciting curiosity regarding this field of research that still needs input of new ideas, models and theories to better reproduce natural phenomena.

One of the current challenges is to predict the occurrence of a shower that has never been observed before. This paper presents the prediction of a meteor shower outburst caused by comet 15P/Finlay, known to be a Near-Earth object. Despite a promising orbital configuration, no meteor shower associated with 15P/Finlay has been found in observation databases so far (or at least prior to 2000, cf. Beech et al., 1999). **Because a low encounter velocity with Earth, meteors produced by comet Finlay will necessarily be fainter than usual showers for equivalent meteoroid mass. We infer that Finlay caused meteors might hardly be detectable by meteor observers.** More recently, a search among the records of the Canadian Meteor Orbit Radar (CMOR) database did not reveal the existence of any past "Finlayid" activity (Ye et al., 2015). However, Ye et al. (2015) reported a possible southern shower on the 6th-7th of October 2021, based on their own work as well as those performed by Mikiya Sato[a], Mikhail Maslov[b], as well as Shanov and Dubrovski (cited in Jenniskens, 2006). These predictions are reminded in Table 1.

In this paper we present the result of our modelling of meteoroid streams ejected by comet 15P/Finlay during its latest apparitions. We predict a meteor shower in 2021, caused by the trails ejected in 2008 and 2014. In Section 2, the orbital evolution of 15P/Finlay is investigated. Section 3 present our meteor shower forecast. These predictions are finally discussed in Section 4.

2 Comet 15P/Finlay

Comet Finlay is a Jupiter family comet (period of 6.5 years) discovered in 1886 by W.H. Finlay, and observed during 13 passages in total. Its orbit is therefore well known and constrained for this period of time (see Table 2). The nucleus of the comet was estimated to 0.92 ± 0.05 km (Fernández et al., 2013). Ishiguro et al. (2016) points out that the comet is known to show irregular activity and to experience several activity outburst, the latest happening in 2014 and 2015. They found a dust production rate of $10^8 - 10^9$ kg per outburst for less than mm-size particles. This is comparable to the production of comet 55P/Tempel-Tuttle, parent body of the Leonids meteor shower (Vaubaillon et al., 2005b). Therefore the comet is theoretically able to produce a meteor shower at Earth, provided our planet enters the meteoroid stream.

Before performing any meteor shower prediction, the ephemeris of the parent body must be established, either from observations or from numerical integration of its orbit as a function of time. We therefore start investigating the orbital stability of 15P/Finlay. A thousand of comet clones are generated using the covariance matrix provided in JPL 142/2, corresponding to the solution of Table 2. Each clone of the comet is integrated

[1]IMCCE, Observatoire de Paris, PSL Research University, CNRS, Sorbonne Universit/'es, UPMC Univ. Paris 06, Univ. Lille., France. Email: jeremie.vaubaillon@obspm.fr

[2]The University of Western Ontario, London, Ontario, Canada; Centre for Planetary Science and Exploration, The University of Western Ontario, London, Ontario N6A 5B8, Canada; IMCCE, Observatoire de Paris, PSL Research University, CNRS, Sorbonne Universit/'es, UPMC Univ. Paris 06, Univ. Lille., France. Email: auriane.egal@obspm.fr

[3]Institut Poytechnique des Sciences Avancées IPSA, 63 boulevard de Brandebourg, F-94200 Ivry-sur-Seine, France, IMCCE, Observatoire de Paris, PSL Research University, CNRS, Sorbonne Universit/'es, UPMC Univ. Paris 06, Univ. Lille., France. Email: josselin.desmars@obspm.fr

[4]IMCCE, Observatoire de Paris, PSL Research University, CNRS, Sorbonne Universit/'es, UPMC Univ. Paris 06, Univ. Lille., France. Email: kevin.baillie@obspm.fr

IMO bibcode WGN-482-vaubaillon-finlay
NASA-ADS bibcode 2020JIMO...48...29V

[a]https://groups.yahoo.com/neo/groups/meteorobs/conversations/messages/44030?guccounter=1, accessed on the 29th Nov. 2019

[b]http://feraj.ru/Radiants/Predictions/1901-2100eng/Finlayids1901-2100predeng.html

Table 1 – Previous predictions of the 2021 encounter with 15P/Finlay's meteoroid trails summarized in Table 4 of Ye et al. (2015).

Modeler	Peak Time	Radiant	vg	ZHR
Maslov	2021 Oct. 7, 01:19	255.8°, −48.3°	10.7	5–50
Sato	2021 Oct. 7, 01:10	255.7°, −48.4°	10.7	...
Ye	2021 Oct. 7, 00:34-01:09	255.6°, −48.4°	10.7	...
Ye	2021 Oct. 6, 21:59-22:33	256.3°, −48.5°	10.7	...

Table 2 – Orbital elements of comet 15P/Finlay, from JPL/HORIZONS.

Epoch	2013-Apr-24 TDB
semi-major axis	3.4867 AU
eccentricity	0.7204
inclination	6.8037°
node	13.8006°
argument of perihelion	347.5656°
mean anomaly	267.3628°

backwards for more than 500 years, using a 15th order RADAU integrator (Everhart, 1985) with an external time step of 1 day. The force model for the integration includes the gravitational attraction of the Sun, the eight planets of the Solar System, the Moon and Pluto, as well as the relativistic corrections to bring to the trajectories. Non-gravitational forces (NGF) due to cometary outgassing were optionally included. **Other non-graviational forces such as radiation pressure or Poynting-Robertson are neglected on the basis that their effect is too small to be significant at such time scale.**

Figure 1 describes the past orbital evolution of the swarm of 15P clones. For each orbital element, the evolution of the nominal clone when considering (grey solid line) or excluding (black curve with open circles) cometary non-gravitational forces is presented. Both trajectories reflect the influence of jovian perturbations on the global evolution of the comet. The discrepancy between both NGF models becomes significant after 330 years of integration.

The dispersion of the swarm of clones, represented by the standard deviation of each orbital element, is illustrated by the limiting lines (black solid curves) above and below the nominal clone solution without NGF of Figure 1. Sudden and significant variations of the clones standard deviation are mainly induced by close encounters with planets, resulting in abrupt dispersion of the simulated particles. After a first increase around 1744 AD, the clones dispersion increases drastically around 1648 AD because of a close encounter with Jupiter. Be-

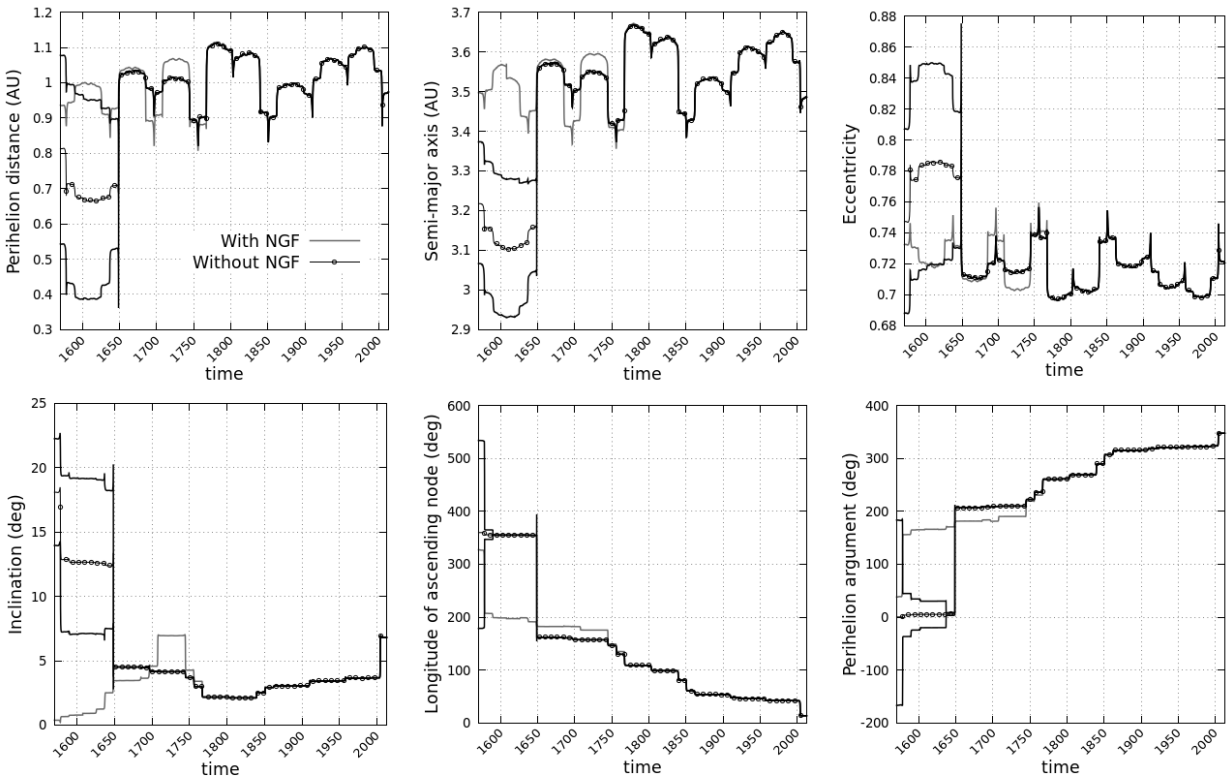

Figure 1 – Dynamical evolution of comet 15P/Finlay over 500 years. The orbital evolution of the nominal clone is represented by the grey solid line (integration with NGF) or black dotted line (integration without NGF). The clones standard deviation σ is illustrated by the black solid lines above and below the nominal solution without NGF (nominal solution ± 1-σ).

fore this date, the comet ephemeris is highly uncertain and should not be considered without a careful analysis.

3 Predictions for 2021

In order to perform the meteor shower prediction we used the models developed by Vaubaillon et al. (2005a); Vaubaillon (2017) (hereafter called "JV2005") and Egal et al. (2018, 2019) (hereafter "AE2019"). The two sets of simulations consider every perihelion passage of the comet between 1886 and 2014, and 1905 to 2014 respectively. As concluded in Section 2, the ephemeris of the comet is reliable over this time span. The simulations involved 570 000 and 3 468 000 particles respectively.

Figure 2 presents a compilation of the nodal crossing location of all the particles crossing the ecliptic plane in 2021. Different colours refer to different ejection epochs. If no enhanced activity can be directly predicted from this Figure (most of the particles cross the ecliptic plane when the Earth is far from their location), it illustrates the high perturbations meteoroid trails suffer after their ejection.

In the line of Jenniskens (2006), Maslov[c] and M. Sato[d] we find that the Earth will encounter the meteoroid stream ejected by comet 15P/Finlay in 2021. However we also find multiple outbursts of varying strength and time. **However we did not find an encounter with the 1988 trail, unlike Maslov.**

Figures 3, 4 and 5 show the location of the nodes of the meteoroids ejected during the 1995, 2014 and 2008 passages of the comet, respectively responsible for the first, second and third peaks, obtained from the method of JV2005. The distribution of radiants are shown in Figures 6, 7 and 8. A summary of the encounter circumstances is presented in Table 3.

For comparison sake, Figure 9 shows the structure of the stream close to Earth around the expected peaks obtained with the AE2019 model. Particles crossing the ecliptic plane at less than 0.001 AU from Earth's orbit, and within ± 3 days of the planet's location (coloured particles) were retained for this analysis. The encounter geometry with the 1995, 2008 and 2014 trails is similar to what observed in Figures 3, 4 and 5. The apparent weaker density of particles in Figure 9 is mainly due to a more restrictive selection of the simulated meteoroids. In this model, the 1995 trail is expected to approach Earth in September 2021, producing a weak activity around September 28 to 29 ($L_\odot$ from 185.46° to 186.32°). The 2008 and 2014 trail are expected to produce a stronger activity on October 6 to 7, 2021. As found with the JV2005 model, the 2014 trail is concentrated at the beginning of October 7, producing a sharper peak of activity. From a first approximation, the 2008 trail might be involved in a weak activity a few hours later. In these simulations, the existence of a fourth wide and low activity caused by the 2002 trail is also found. This peak occurs on October 8th, after a slow rise of activity lasting 3 days in total. The level is less than the peak caused by the 2008 trail.

The accurate prediction of a shower duration, peak time and intensity depends on several criteria, like the threshold distance with Earth's orbit, the relative time passage with the planet or the weighting scheme applied to the simulated meteoroids (cf. Vaubaillon et al., 2005a or Egal et al., 2019) In this analysis, this process is even harder since no meteor shower associated to comet 15P/Finlay has been observed in the past. Figure 10 illustrates how the duration and shape of the shower intensity profile evolve with the weights applied to the particles. The grey curve represents the flux variation when the same weight is attributed to all the particles (called "unweighted" solution). The black dotted curve represents the output of Egal et al. (2019) weighting scheme for a meteoroids size distribution index at ejection of 2.5 (called "weighted" solution). Each peak time is conserved after the application of the different weights. However, the duration and shape of the 6-7 October activity differ from one solution to another, and the suspected fourth peak caused by the 2002 trail on October 8 disappears in the weighted solution. The relative contribution of each trail to the profile is presented in Figure 11. We see that our weighting scheme increased the estimated intensity of the 2014 and 1995 trails, while lowered down the contribution of the 2008 and 2002 trails.

From these simulations, four peaks of activity might be observable in September-October 2021, around the solar longitudes 186.077° (1995 trail), 193.677° (2014 trail), 193.785° (2008 trail) and 194.527° (2002 trail). The main activity is expected to be caused by the 2014 trail, which should be at least twice as large as all the other peaks. However, no reliable ZHR can be estimated from this model without a proper calibration based on meteor measurements at this stage. For more realistic estimates of the ZHR, the reader is referred to the values presented in Table 3, where the simulated meteoroid flux obtained with JV2005 model has been calibrated on the photometry of the comet. However, even with such a model, the size distribution of $> 100\,\mu m$ is unknown since visible photometry of comet coma is performed for $\simeq$ µm-size particles.

3.1 Shower visibility geometry

The mean location of the radiants puts the shower in the constellation of Ara. The orientation of the Earth and the location of the sub-radiant points are shown in Figs 12, 13 and 14. The location of the radiants and the corresponding time of maxima are provided in Table 3.

4 Discussion and conclusion

The meteors will enter the Earth at a very low velocity of 10.8 $km.s^{-1}$, so only the largest ones will cause visible meteors. From Fig.3 we can forecast that the activity of the first peak will be broad, lasting nearly an entire day. This will ease its observation from nearly any point in the Southern hemisphere. However, an expected ZHR of $13\,hr^{-1}$ (Table 3) will make it hard to

[c] http://feraj.ru/Radiants/Predictions/1901-2100eng/Finlayids1901-2100predeng.html

[d] https://groups.yahoo.com/neo/groups/meteorobs/conversations/messages/44030?guccounter=1, accessed on the 29th Nov. 2019

Table 3 – Circumstances of encounter between the Earth and meteoroid trails ejected from comet 15P/Finlay (from model JV2005). trail: year of ejection of the considered trail intersecting the Earth in 2021. dist: mean distance of the trail to the Earth. SolLong: Solar Longitude at the time of maximum; V_{geo}: expected geocentric velocity; α, δ: coordinates and standard deviation of the radiant; ZHR: zenithal hourly rate (see also section 4); conf_id : confidence index as defined by Vaubaillon (2017).

trail year	dist AU	SolLong deg	date UT	α deg	δ deg	V_{geo} km.s^{-1}	ZHR h^{-1}	conf_id —
1995	0.00125	186.072	2021-09-29T08:35	260.8 ± 0.9	-57.4 ± 0.5	10.807	13	SYO0/1CE0.00
2008	−0.00143	193.728	2021-10-07T03:55	254.5 ± 1.0	-48.3 ± 0.2	10.730	41	SYO0/1CE0.00
2014	0.00028	193.674	2021-10-07T00:35	255.5 ± 0.8	-48.3 ± 0.6	10.752	178	SYO0/1CE0.00

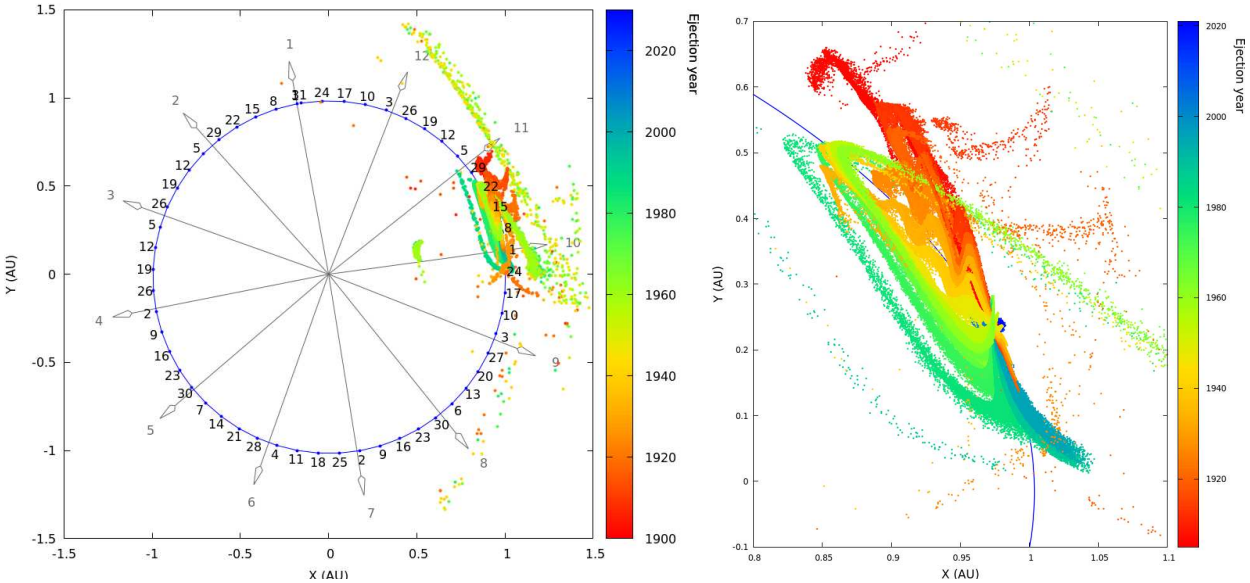

Figure 2 – Location of meteoroids ejected from 15P/Finlay crossing the ecliptic plane in 2021 (from model AE2019). Different colours refer to different ejection dates. Grey arrows point towards the Earth's location at the beginning of each month (varying from 1 to 12). The position of the planet every 7 days from these dates are indicated by blue dots and their corresponding number.

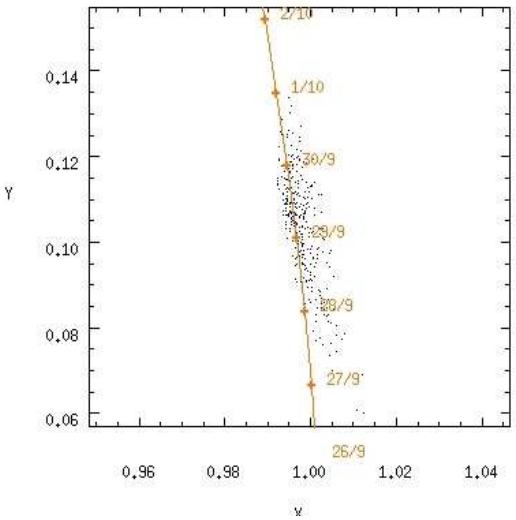

Figure 3 – Meteoroid trail ejected in 1995 configuration with respect to the Earth (from model JV2005), causing the first peak of the 2021 meteor outburst caused by comet 15P/Finlay.

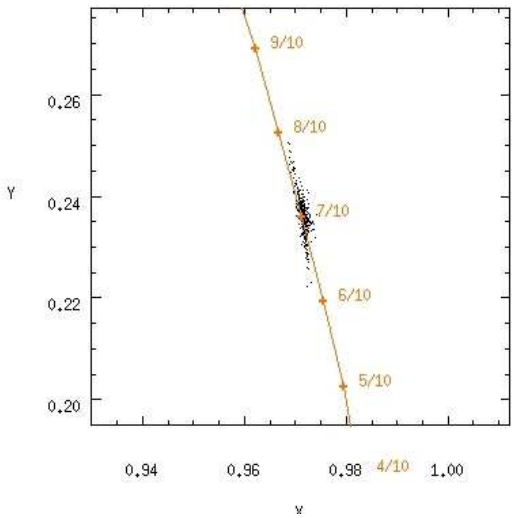

Figure 4 – Meteoroid trail ejected in 2014 configuration with respect to the Earth (from model JV2005), causing the second peak of the 2021 meteor outburst caused by comet 15P/Finlay.

distinguish from sporadic background. Ideally a global effort to follow the outburst from beginning to end is required. The peak will be best observed at its central part from New-Zealand, as seen in Figure 12.

Presumably the 2nd and 3rd peaks will be easier to spot w.r.t. sporadic background thanks to a higher ZHR. They might both be observed from a single area located either at the Northern-most tip of Antarctica or

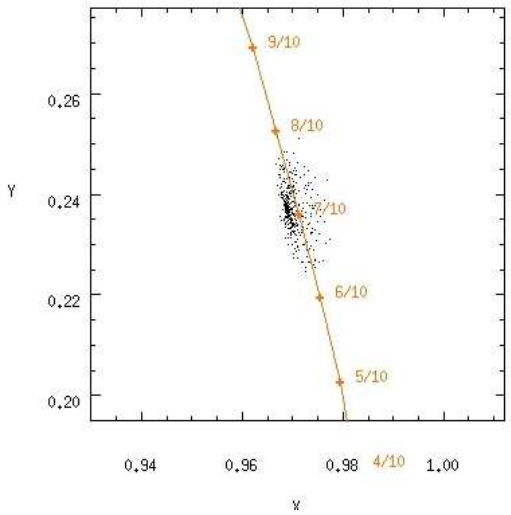

Figure 5 – Meteoroid trail ejected in 2008 configuration with respect to the Earth, causing the third peak of the 2021 meteor outburst caused by comet 15P/Finlay.

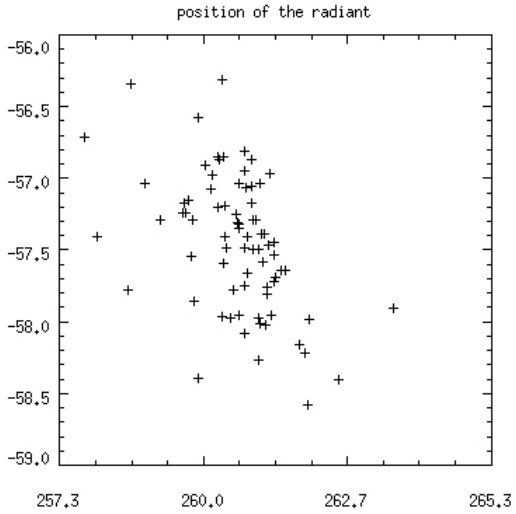

Figure 6 – Theoretical radiant distribution of the first peak (from model JV2005).

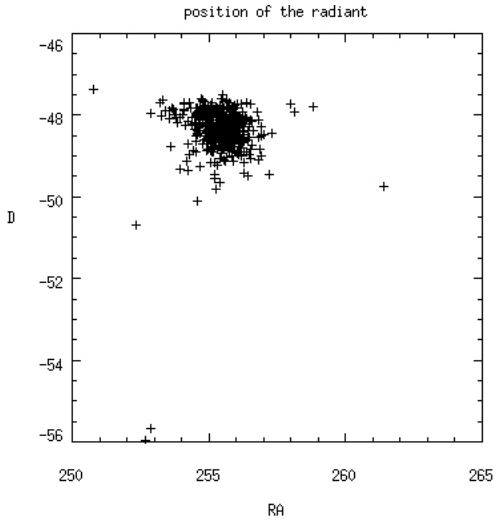

Figure 7 – Theoretical radiant distribution of the second peak (from model JV2005).

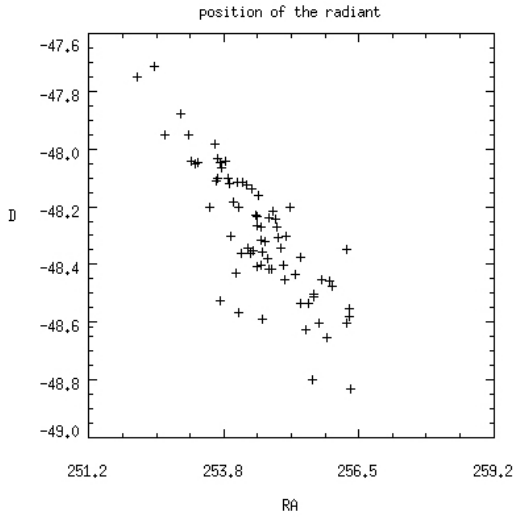

Figure 8 – Theoretical radiant distribution of the third peak (from model JV2005).

the Southern-most tip of the American continent (Figures 13 and 14).

The ratio between < 1 mm and > 1 mm simulated particles for model JV2005 are: 10:1 for the 1995 trail, 100:1 for the 2008 trail, and nearly 1:1 for the 2014 trail. The extreme low velocity will affect the visibility of the showers in the visible spectrum. As a consequence, the most likely visible shower is that caused by the 2014 trail.

Observers should keep in mind that the level of the showers have large uncertainties since this will be the first observed meteor shower from comet 15P/Finlay. The comet outburst in 2014 makes the predicted third peak the most exciting outburst to observe. However the two other peaks are mandatory to record in order to quantify the change of activity of the comet before and after the outburst. Although the comet outburst in 2014 was witnessed and recorded, the exact amount of large meteoroids (causing visible meteors) is unknown.

We conclude as a call to observers to report their measurements to the International Meteor Organization[e].

5 Acknowledgements

Part of the calculations used the CINES supercomputer facility, France. Simulations performed by A. Egal were supported in part by NASA Meteoroid Environment Office under cooperative agreement 80NSSC18M0046 and contract 80MSFC18C0011.

References

Beech M., Nikolova S., and Jones J. (1999). "The 'silent world' of Comet 15P/Finlay". *MNRAS*, **310:1**, 168–174.

Egal A., Wiegert P., Brown P. G., Moser D. E., Campbell-Brown M., Moorhead A., Ehlert S., and Moticska N. (2019). "Meteor shower modeling:

[e] https://www.imo.net

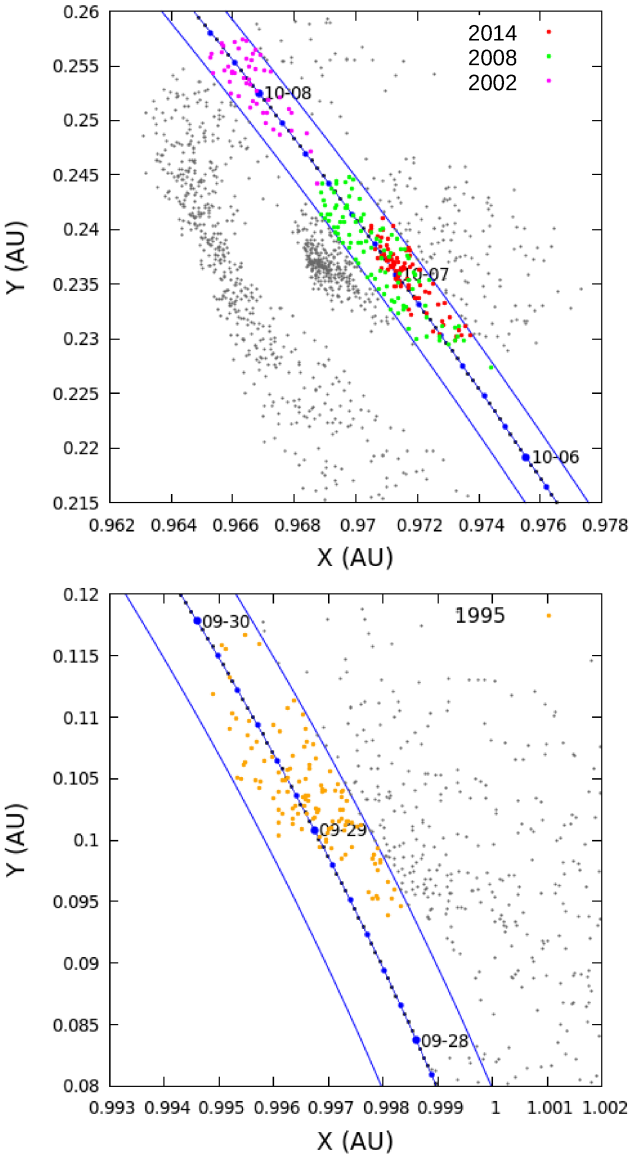

Figure 9 – Nodal crossing location of meteoroids simulated using AE2019 model around September 29, 2021 (bottom panel) and October 7, 2021 (top panel). The dashed blue curve represents the Earth's successive locations in 2021, while solid lines mark the region considered for the analysis. Meteoroids retained are colour-coded in function of their ejection epoch.

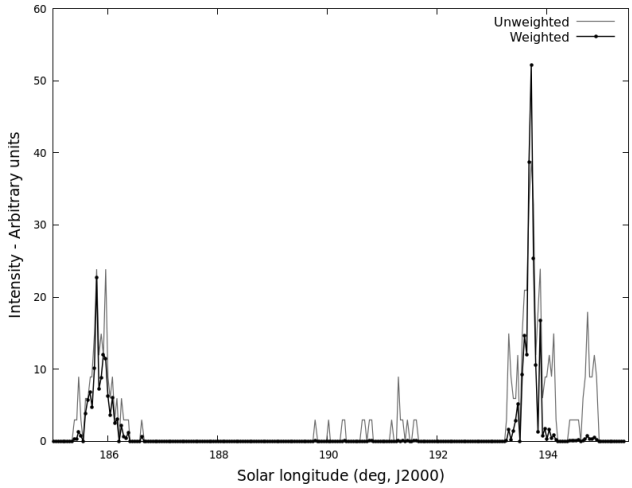

Figure 10 – Influence of the weighting scheme on the activity profile of the shower (from model AE2019).

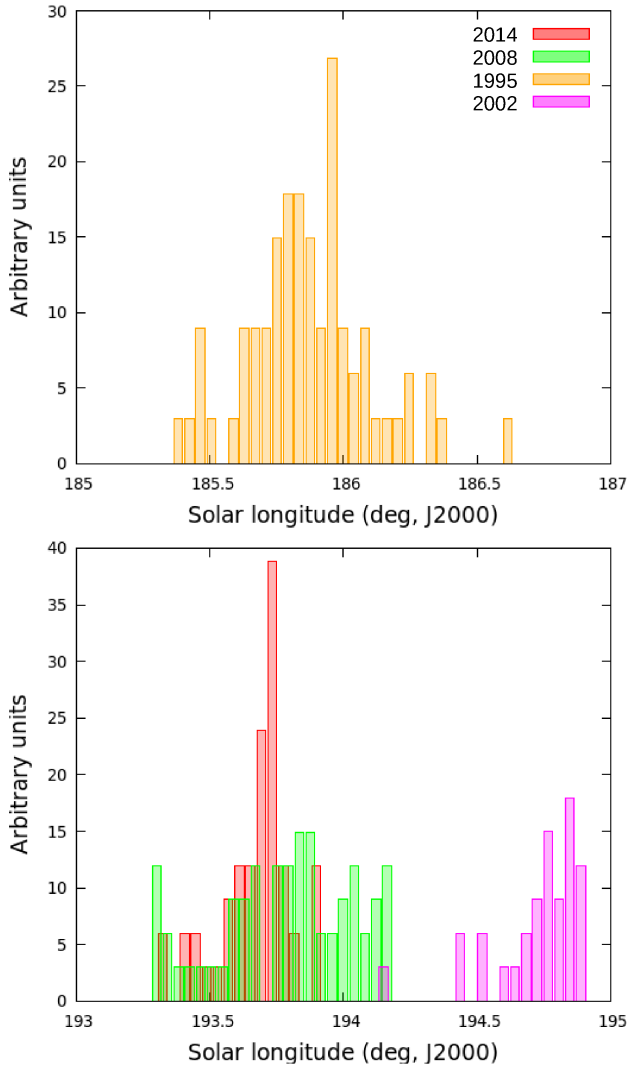

Figure 11 – Relative contribution of each trail to the unweighted profile of Figure 10 (from model AE2019).

Past and future Draconid outbursts". *Icarus*, **330**, 123–141.

Egal A., Wiegert P., Brown P. G., Moser D. E., Moorhead A. V., and Cooke W. J. (2018). "The Draconid Meteoroid Stream 2018: Prospects for Satellite Impact Detection". *ApJ*, **866:1**, L8.

Everhart E. (1985). "An efficient integrator that uses Gauss-Radau spacings". *International Astronomical Union Colloquium*, **83**, 185–202.

Fernández Y. R., Kelley M. S., Lamy P. L., Toth I., Groussin O., Lisse C. M., A'Hearn M. F., Bauer J. M., Campins H., Fitzsimmons A., Licand ro J., Lowry S. C., Meech K. J., Pittichová J., Reach W. T., Snodgrass C., and Weaver H. A. (2013). "Thermal properties, sizes, and size distribution of Jupiter-family cometary nuclei". *Icarus*, **226:1**, 1138–1170.

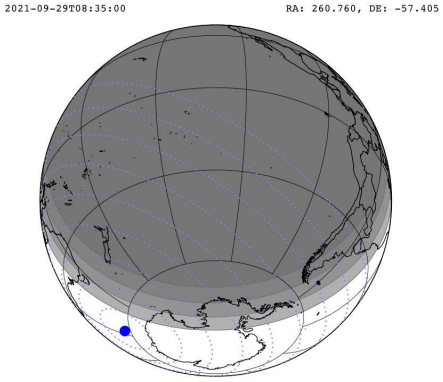

Figure 12 – Sub-radiant location of the first peak (blue dot). Earth surface in the night is represented in gray colour with different level of grey corresponding to civil, nautical and astronomical twilights. The dotted blue lines represents the isoelevation lines of the radiant every 10 degrees.

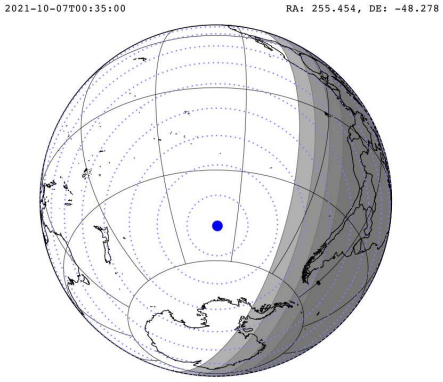

Figure 13 – Sub-radiant location of the second peak. See Fig. 12.

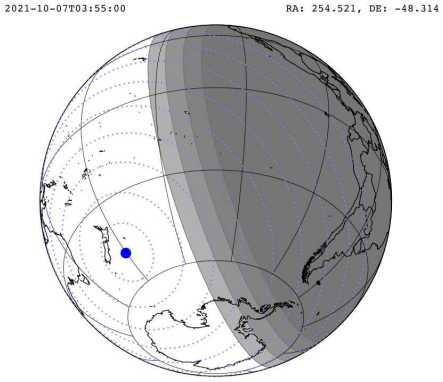

Figure 14 – Sub-radiant location of the third peak. See Fig. 12

Ishiguro M., Kuroda D., Hanayama H., Kwon Y. G., Kim Y., Lee M. G., Watanabe M., Akitaya H., Kawabata K., Itoh R., Nakaoka T., Yoshida M., Imai M., Sarugaku Y., Yanagisawa K., Ohta K., Kawai N., Miyaji T., Fukushima H., Honda S., Takahashi J., Sato M., Vaubaillon J. J., and Watanabe J.-i. (2016). "2014-2015 Multiple Outbursts of 15P/Finlay". *AJ*, **152:6**, 169.

Jenniskens P. (2006). *Meteor Showers and their Parent Comets*. Cambridge University Press.

Jenniskens P. and Lyytinen E. (2019a). "Alpha Monocerotids 2019". *Central Bureau Electronic Telegrams*, **4692**, 1.

Jenniskens P. and Lyytinen E. (2019b). "Alpha Monocerotids Meteors 2019". *Central Bureau Electronic Telegrams*, **4699**, 1.

Vaubaillon J. (2017). "A confidence index for forecasting of meteor showers". *Planet. Space Sci.*, **143**, 78–82.

Vaubaillon J., Colas F., and Jorda L. (2005a). "A new method to predict meteor showers. I. Description of the model". *A&A*, **439:2**, 751–760.

Vaubaillon J., Colas F., and Jorda L. (2005b). "A new method to predict meteor showers. II. Application to the Leonids". *A&A*, **439:2**, 761–770.

Vaubaillon J., Neslušan L., Sekhar A., Rudawska R., and Ryabova G. O. (2019). "From Parent Body to Meteor Shower: The Dynamics of Meteoroid Streams". In Ryabova G. O., Asher D. J., and Campbell-Brown M. J., editors, *Meteoroids: Sources of Meteors on Earth and Beyond*, Cambridge, UK. Cambridge University Press, pages 161–186.

Ye Q.-Z., Brown P. G., Bell C., Gao X., Mašek M., and Hui M.-T. (2015). "Bangs and Meteors from the Quiet Comet 15P/Finlay". *ApJ*, **814:1**, 79.

Handling Editor: Javor Kac
This paper has been typeset from a LaTeX file prepared by the authors.

Three components of 'Taurids' II

Masahiro Koseki[1]

This study confirms SE and SF components in the Southern Taurids (Koseki, 2012a). The SF component generally changes its appearance year by year, corresponding to the activity of a 7:2 resonant swarm with Jupiter. The SE component represents the average annual activity and its activity is comparable to SF in those years. The 'Southern Taurids' are a composite of the SE and SF components and the very long period referred to in the IAU meteor shower list is the combined apparent activity period; the SE component moves more slowly in Sun centered ecliptic coordinates ($\lambda - \lambda_s$, β) than SF and, therefore, the SF component catches up and passes over the SE component.
Showers #257ORS (Southern χ Orionids) and #286FTA (ω Taurids) cause confusion in the late 'Southern Taurid' activity, the mixed radiant area becoming a long ellipse in the end stage. ORS seems an independent activity though its companion #256ORN is a conglomerate of sporadics and late Northern Taurids. FTA could be regarded as the latest activity of 'Southern Taurids' though 11 years of data are still not enough to allow a clear conclusion.

Received 2020 March 17

Note: The author used 'S_E' and 'S_F' in the former paper because their activities were under question. We confirm them in this study and can now call them simply SE and SF activities without using subscripts.

1 Introduction

'Taurids' are one of the most intense activities of the antihelion source ANT but there is substantial confusion in the IAUMDC shower database (SD). It is easy to illustrate this confused situation by displaying radiant distributions firstly of video meteors of the SonotaCo network (SonotaCo, 2009) including 2007–2018 observations (Figure 1) and secondly of the SD (Figure 2). The video meteors are distributed over a long elliptical area and the distribution of the SD showers seems to reflect the observed ellipse. Table 1 lists all SD showers drawn in Figure 2. We recognize large differences within Southern Taurids (STA) and Northern Taurids (NTA) in the SD, and in addition to them there are many 'mini' showers registered in the SD.

The author showed there are three components in 'Taurids' activity (Koseki, 2012a) based mainly on photographic observations; the Southern branch with two components (SE and SF; see Figure 15 later) and the Northern branch (NTA). Video observations have accumulated a very large amount of meteor data, about two hundred times more abundant than photographic data. We can confirm precisely the former hypothesis and check the showers that are listed as independent showers in the SD.

We know Southern Taurids have a long 'tail' after the maximum; the radiant distribution shows a long enduring slender shape (see Figures 3 and 4). The author had completed surveying almost every entry in the SD by constructing the radiant distributions and the activity profiles (see Section 2.2 for the activity profile). There are two interesting activities in those figures, i.e., 0257ORS04 (Figure 3) and 0286FTA01 (Figure 4); here we refer to each entry as shower number + 3 character code + additional entry number for that shower in the SD. It seems to be interesting to add these two activities into this study.

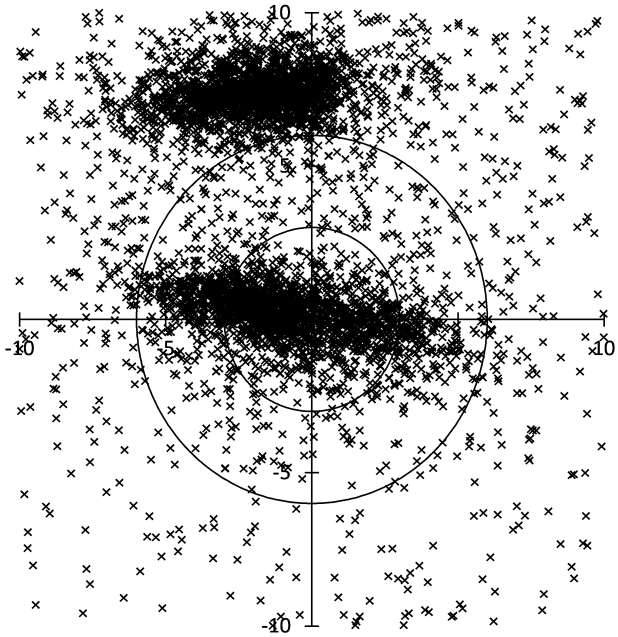

Figure 1 – Radiant distribution of SonotaCo net video observations 2007–2018 centered at ($\lambda - \lambda_s$, β) = (190.7, −5.0) between solar longitudes λ_s= 213.4–233.4. The y-axis runs through each ecliptic longitude of $\lambda - \lambda_s$ and the scale is in degrees. Two circles represent the distance 3° and 6° from the center. The central elliptical distribution is STA and the top is NTA.

2 Preliminary search

We cannot set the search condition uniformly, because the intensity of their activities and the distance from the neighboring activities differ in every case. We must start to select proper conditions firstly to study the 'Taurid' complex correctly. We choose the preliminary search condition, that is, the radiant point and the activity period for each activity as listed in Table 2 and try to settle the best condition to get reliable results. It is necessary to explain how to calculate the radiant

[1]The Nippon Meteor Society (NMS), 4-3-5 Annaka, Annaka-shi, Gunma-ken, 379-0116 Japan. Email: geh04301@nifty.ne.jp

IMO bibcode WGN-482-koseki-taurids
NASA-ADS bibcode 2020JIMO...48...36K

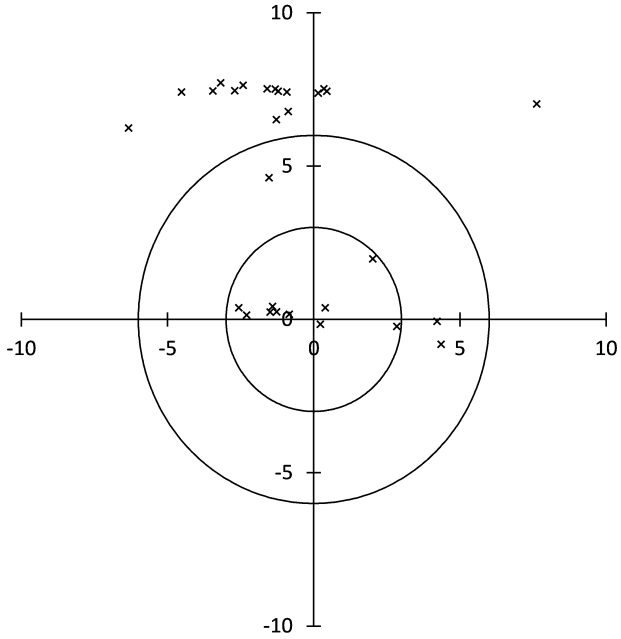

Figure 2 – Radiant distribution of the showers listed in the SD; the position in ecliptic coordinates and the period in solar longitude are same as Figure 1.

Table 1 – Meteor showers of the SD plotted in Figure 2; centered at $(\lambda - \lambda_s,\ \beta) = (190.7,\ -5.0)$ between $213.4 < \lambda_s < 233.4$.

Code	λ_s	$\lambda - \lambda_s$	β	V_g
0017NTA02	214.1	193.9	2.7	29.6
0626LCT01	215	192.2	−4.8	27.4
0002STA05	216	193.0	−4.8	26.6
0626LCT00	216	193.3	−4.6	27.9
0631DAT00	216	195.2	2.4	29.3
0631DAT01	216.2	194.1	2.5	29.0
0017NTA07	218.4	192.0	1.5	27.7
0017NTA05	219	192.2	−0.4	28.1
0002STA03	219.7	191.5	−4.8	27.2
0017NTA06	220	192.0	2.5	28.0
0630TAR00	220	193.1	2.6	28.1
0630TAR01	221.6	193.4	2.5	28.9
0628STS00	223	192.0	−4.7	28.2
0628STS01	223	192.1	−4.6	28.6
0002STA00	224	186.5	−5.0	28
0017NTA00	224	197.0	1.3	28.3
0017NTA01	224	183.1	2.0	30.69
0017NTA03	224.5	191.6	1.8	28.1
0637FTR01	224.5	190.5	−5.2	26.7
0637FTR00	225	190.3	−4.6	27.4
0632NET01	225.4	192.3	2.5	28.3
0632NET00	227	191.9	2.4	28.0
0635ATU01	228.8	191.6	2.4	28.4
0625LTA00	231	187.8	−5.2	25.7
0635ATU00	231	190.5	2.4	27.4
0285GTA00	232.8	188.7	−3.0	14.1
0625LTA01	232.8	186.3	−5.8	24.1
0629ATS00	233	190.2	2.4	27.5
0629ATS01	233	190.4	2.5	27.6

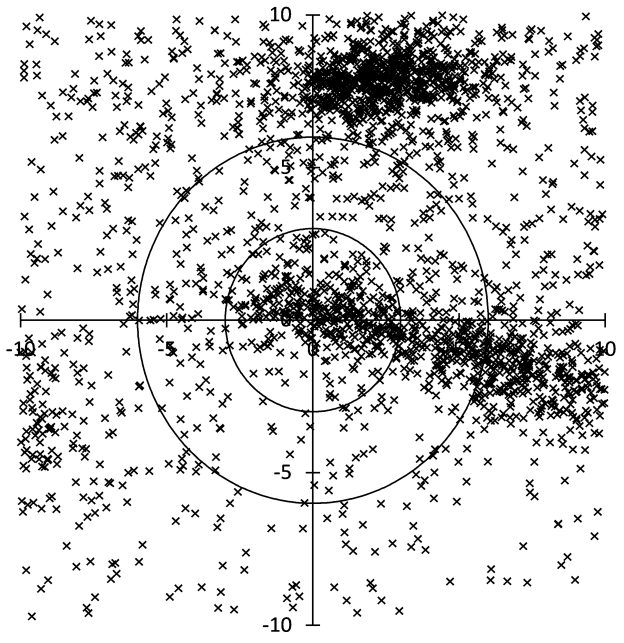

Figure 3 – Radiant distribution of SonotaCo net video observations 2007–2018 centered at $(\lambda - \lambda_s,\ \beta) = (190.3,\ -5.2)$ between $\lambda_s = 237.6$–257.6; ORS.

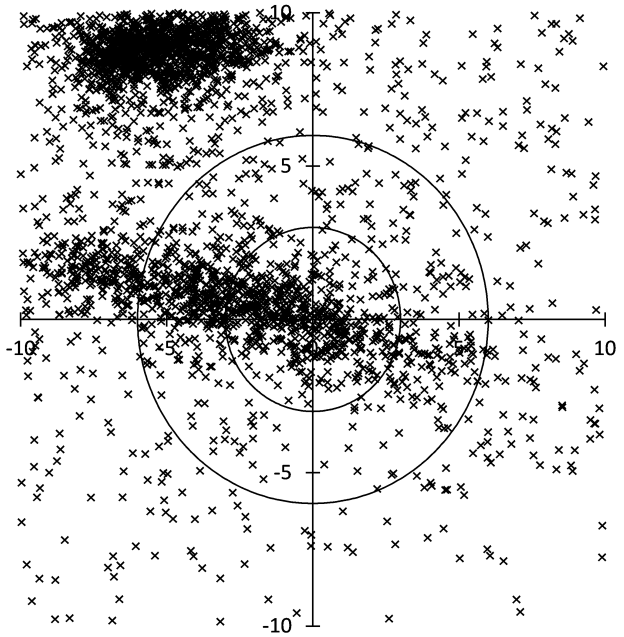

Figure 4 – Radiant distribution of SonotaCo net video observations 2007–2018 centered at $(\lambda - \lambda_s,\ \beta) = (184.0,\ -6.3)$ between $\lambda_s = 232.0$–252.0; FTA.

drift, the size of radiant and the activity period prior to studying their individual character.

2.1 Estimation of radiant drift

A meteor shower radiant usually shifts with time in equatorial coordinates but is almost stationary for the Sun centered ecliptic coordinates $(\lambda - \lambda_s,\ \beta)$ in general. The radiant shift can be represented as a short line in the orthographic projection of the $(\lambda - \lambda_s,\ \beta)$ coordinates even if the radiant moves in the $(\lambda - \lambda_s,\ \beta)$ coordinates; Taurids are such a case (Figure 1).

We calculate the linear regression of x and y on λ_s for the period listed in Table 2; $(x,\ y)$ are the coordi-

Table 2 – Conditions for the preliminary search; radiant points of three components are based on Koseki (2012a) and additional two showers from the SD; the search periods ($\Delta\lambda_s$) are set $\pm10°$ from λ_s. Δr is the search radius in degrees from the radiant point.

Code	λ_s	$\lambda - \lambda_s$	β	Δr	$\Delta\lambda_s$
SF	223.4	190.7	−5.0	3	213.4–233.4
SE	202.6	194.8	−4.4	3	192.6–212.6
0257ORS04	247.6	190.3	−5.2	3	237.6–257.6
0286FTA01	242.0	184.0	−6.3	3	232.0–252.0
NTA	226.3	191.7	2.1	3	216.3–236.3

nates of individual radiants centered at the shower radiant. The regression calculations were repeated several times to become stable.

2.2 Estimation of activity period: activity profile drawn by radiant density

We can count the number of radiant points according to the distance from the drift compensated estimates of the radiant in ($\lambda - \lambda_s$, β). Nr ≤ 3 is the number of meteors within 3° from the estimated radiant in each 1° bin of λ_s.

These raw meteor numbers fluctuate widely with the observational conditions, though we use 11 years observations of SonotaCo net (SonotaCo, 2009). It is necessary to use other indexes to express the shower activity profiles; Koseki (2019) proposes to use the radiant density ratios; DR3 is the density ratio within a circle of 3° radius relative to a ring of 3–6°; DR10 is the density ratio within a circle of 3° relative to a ring of 6–10°; DR15 is the density ratio within a circle of 3° relative to a ring of 10–15°. It is better to use the sliding mean of the radiant density ratios within bins of 3° in λ_s in order to avoid shortages of meteor numbers in the reference areas.

Which index is the best is different case by case; DR15 seems to give the best expression for the SF component (Figure 10) and DR3 for ORS (Figure 12).

2.3 SF component

The author pointed out that there are two components, i.e., SE and SF components in STA (Table 3 of Koseki 2012a); the SF component coincides with the maximum of Taurid activity in visual observations. It seems to be appropriate to study the SF component at first. We searched SF component members under the condition given in Table 2 taking radiant drift into account as described in Section 2.1. We repeated the calculation until the results are stable; Figure 5 is the radiant distribution after 6 iterations. It is clear the intrinsic radiant distribution of the SF component is circular, not elongated as shown in Figure 1 and, moreover, the larger part of radiants are located within 3° from the center. We can confirm the initial search period $213.4 < \lambda_s < 233.4$ is proper and, therefore, it seems to be proper to exclude meteors within 3° from the center and between $213.4 < \lambda_s < 233.4$ to study other Taurid components.

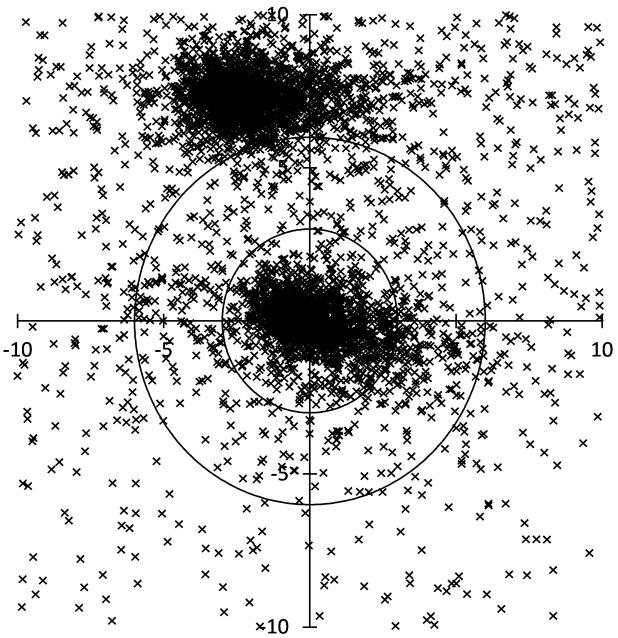

Figure 5 – Radiant distribution of SF component in the period $213.4 < \lambda_s < 233.4$. The center is not stationary but moving according to the result of the linear regression (see text and Table 3).

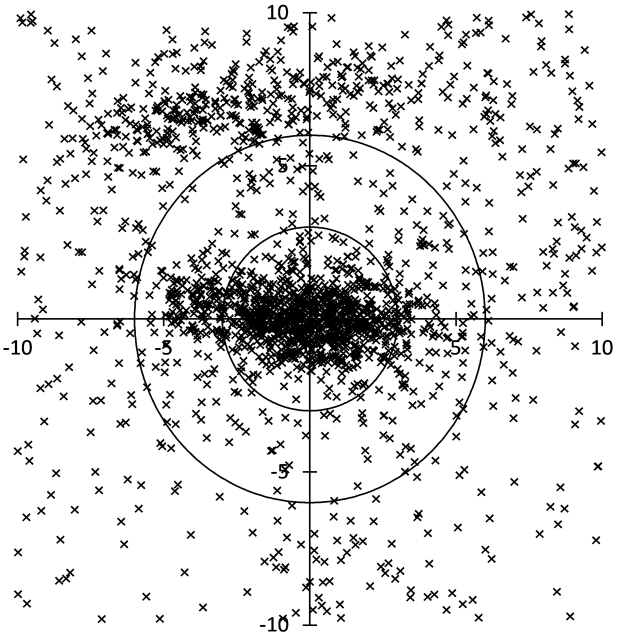

Figure 6 – Radiant distribution of SE component in the period $192.6 < \lambda_s < 212.6$.

2.4 SE component

We searched SE component members subsequently on the basis of Table 2 by excluding SF component members because the SE component is the second constituent of STA activities. Figure 6 shows the radiant distribution after 7 iterations; the shape is not circular but elliptical; or might be accompanied with other weak activities.

2.5 ORS

ORS seems to be nothing but a part of the elongated radiant distribution (Figure 3). We can separate it from

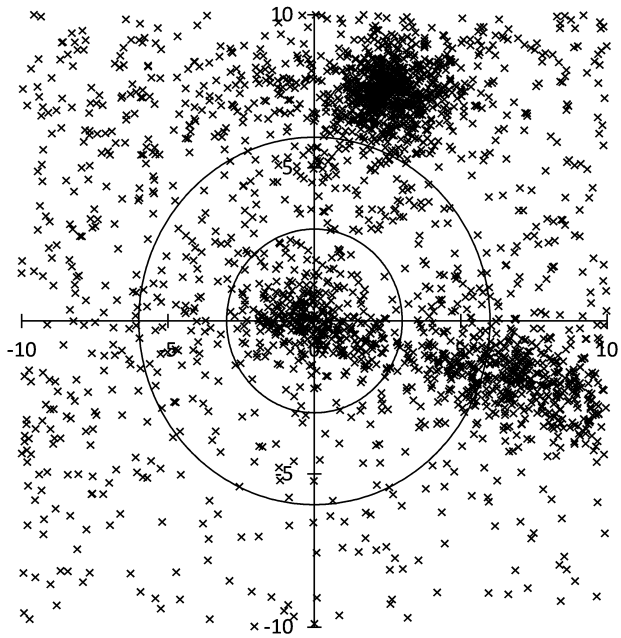

Figure 7 – Radiant distribution of ORS in the period $237.6 < \lambda_s < 257.6$.

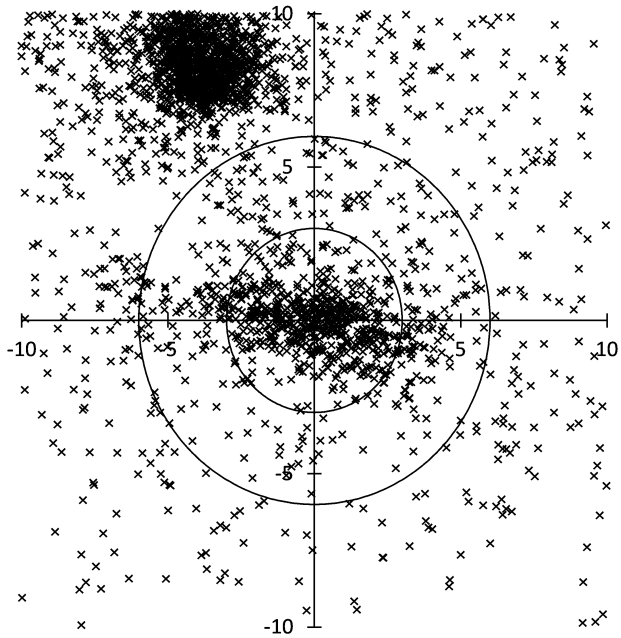

Figure 8 – Radiant distribution of FTA in the period $232.0 < \lambda_s < 252.0$.

sporadics and other STA related activities (Figure 7) after 6 iterations. We excluded meteors within 3° from the center of the ORS radiant and between $237.6 < \lambda_s < 257.6$ to study FTA.

2.6 FTA

FTA looks only a western (right) edge of the elongated radiant distribution (Figure 4) contrary to ORS, but its radiant distribution became smaller after 6 iterations (Figure 8). However, profiles of both DR10 and DR15 strongly suggest FTA might be continuing activity of the SF component (see Figure 13).

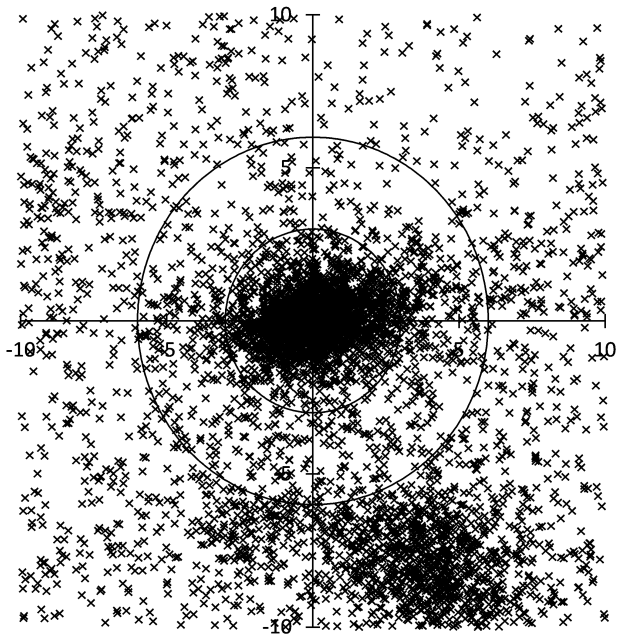

Figure 9 – Radiant distribution of NTA in the period $216.3 < \lambda_s < 236.3$.

2.7 NTA

NTA is a clearly independent activity of the Taurid complex and the result of 6 iterations is also clear (Figure 9); the excluding process described in Sections 2.4 and 2.5 is not necessary for the iterations.

3 Results

The preliminary search gives the general conditions of our targets. We can set the conditions as given in Table 3 that do not overlap each other in place and in time, and can separate each target. We need several additional iterations because of the change of the search condition.

3.1 Radiant drift

It seems unnecessary to give the radiant distributions because the changes of the outlines of them are very small. Tables 4a to 4e show the estimated elements of the components calculated from the radiant drift and the velocity change by additional iterations. The SF component has a unique character; the radiant drift in $(\lambda - \lambda_s, \beta)$ coordinates is the fastest of the five components; on the contrary, it is the slowest of the five in (α, δ) coordinates. This drift originates from the structure of the stream; the ecliptic coordinates of the perihelion of the SF component and the semi major axis of it are almost constant (Table 4a) as Spurný et al. (2017) pointed out.

The radiant distribution of the SE component is rather more diffuse than the SF component even after the iterations (Figure 6), and the radiant moves more slowly than the SF component; it is very interesting that the SF component catches up and passes over the SE component. Its perihelion moves along the ecliptic latitude ($\beta_\Pi = 4.9$) but the longitude changes more slowly than the expectation from the angular velocity of the Earth's revolution around the Sun. If the peri-

Table 3 – Conditions for the verification; a and b are the coefficient and the constant expressed as $\lambda - \lambda_s = a * \lambda_s + b$ or $\beta = a * \lambda_s + b$ of the linear regression obtained by the preliminary search.

Code	$\lambda - \lambda_s$		β		Δr	$\Delta\lambda_s$
	a	b	a	b		
SF	0.41898	−94.31	−0.05970	13.52	2	216.5–226.5
SE	0.18812	−38.76	−0.01808	3.63	3	197.6–207.6
0257ORS04	0.18633	−45.63	−0.02612	6.78	3	242.6–252.6
0286FTA01	0.31826	−77.21	−0.11458	27.66	3	237.0–247.0
NTA	0.26751	−61.21	0.01335	−2.75	3	208.0–248.0

Table 4a – Estimated elements of SF component, as a function of solar longitude λ_s. Columns are radiant coordinates (ecliptic, then equatorial), geocentric velocity, eccentricity, perihelion distance, inclination, argument of perihelion, longitude of ascending node, ecliptic longitude and latitude of the perihelion, and semi major axis.

λ_s	$\lambda - \lambda_s$	β	α	δ	V_g	e	q	i	ω	Ω	λ_Π	β_Π	a
200	202.5	−3.0	41.0	12.7	34.1	0.911	0.169	6.1	138.0	20.0	158.2	4.1	1.89
205	200.2	−3.4	43.7	13.1	32.7	0.892	0.208	6.0	132.7	25.0	157.9	4.4	1.93
210	197.9	−3.8	46.5	13.5	31.3	0.873	0.249	5.8	127.4	30.0	157.5	4.6	1.97
215	195.6	−4.1	49.3	13.9	29.9	0.854	0.293	5.6	122.1	35.0	157.2	4.8	2.00
220	193.3	−4.5	52.0	14.2	28.6	0.834	0.337	5.4	116.8	40.0	157.0	4.8	2.03
225	190.9	−4.8	54.8	14.5	27.2	0.813	0.383	5.2	111.7	45.0	156.7	4.9	2.04
230	188.6	−5.2	57.6	14.8	25.8	0.791	0.428	5.1	106.5	50.0	156.6	4.9	2.05
235	186.3	−5.5	60.3	15.0	24.4	0.769	0.473	4.9	101.5	55.0	156.5	4.8	2.05
240	184.0	−5.8	63.1	15.2	23.0	0.745	0.518	4.7	96.5	60.0	156.6	4.6	2.03
245	181.7	−6.1	65.9	15.4	21.6	0.720	0.561	4.5	91.7	65.0	156.7	4.5	2.00
250	179.4	−6.4	68.7	15.5	20.2	0.693	0.603	4.3	87.0	70.0	157.0	4.3	1.97

Table 4b – Estimated elements of SE component.

λ_s	$\lambda - \lambda_s$	β	α	δ	V_g	e	q	i	ω	Ω	λ_Π	β_Π	a
185	200.4	−4.0	25.0	6.1	30.5	0.858	0.226	6.3	132.6	5.0	137.8	4.6	1.59
190	199.0	−4.1	28.4	7.3	29.9	0.849	0.248	6.1	129.6	10.0	139.8	4.7	1.64
195	197.7	−4.3	31.9	8.4	29.4	0.840	0.271	6.0	126.6	15.0	141.8	4.8	1.69
200	196.3	−4.4	35.4	9.5	28.8	0.831	0.294	5.8	123.6	20.0	143.7	4.8	1.74
205	194.9	−4.5	39.0	10.5	28.2	0.823	0.318	5.6	120.6	25.0	145.7	4.9	1.79
210	193.6	−4.7	42.5	11.4	27.7	0.815	0.342	5.5	117.5	30.0	147.6	4.9	1.84
215	192.2	−4.8	46.1	12.4	27.1	0.807	0.366	5.4	114.5	35.0	149.6	4.9	1.89
220	190.8	−4.9	49.8	13.2	26.6	0.799	0.390	5.2	111.4	40.0	151.5	4.9	1.95
225	189.5	−5.1	53.4	14.0	26.0	0.792	0.414	5.1	108.4	45.0	153.5	4.8	2.00
230	188.1	−5.2	57.1	14.7	25.4	0.785	0.439	5.0	105.4	50.0	155.5	4.8	2.04
235	186.8	−5.3	60.8	15.3	24.9	0.779	0.462	4.8	102.5	55.0	157.5	4.7	2.09

Table 4c – Estimated elements of ORS.

λ_s	$\lambda - \lambda_s$	β	α	δ	V_g	e	q	i	ω	Ω	λ_Π	β_Π	a
230	193.8	−4.7	62.7	16.3	28.5	0.828	0.332	5.7	117.9	50.0	168.0	5.0	1.93
235	192.7	−4.7	66.8	16.9	28.0	0.821	0.351	5.5	115.5	55.0	170.6	5.0	1.96
240	191.6	−4.8	70.8	17.4	27.5	0.814	0.371	5.3	113.0	60.0	173.1	4.9	2.00
245	190.5	−4.9	74.8	17.8	27.0	0.807	0.391	5.2	110.5	65.0	175.6	4.9	2.03
250	189.4	−4.9	78.9	18.1	26.5	0.801	0.411	5.0	108.1	70.0	178.2	4.8	2.06
255	188.3	−5.0	83.0	18.3	26.0	0.794	0.431	4.9	105.7	75.0	180.7	4.7	2.10
260	187.2	−5.1	87.1	18.3	25.5	0.788	0.451	4.8	103.3	80.0	183.3	4.6	2.13
265	186.1	−5.1	91.2	18.3	25.0	0.782	0.471	4.6	100.9	85.0	185.9	4.6	2.15
270	185.0	−5.2	95.3	18.2	24.5	0.775	0.490	2.7	98.6	90.0	188.6	2.7	2.18

helion moves in accordance with the Earth's revolution, the radiant would be fixed in ($\lambda - \lambda_s$, β) coordinates. The structure of the orbit of the SE component seems to be common in ANT activities.

ORS moves more slowly than FTA in ($\lambda - \lambda_s$, β) coordinates; they look like the relation between SE and SF components; initial radiant distributions of ORS and FTA form a long ellipse (Figures 3 and 4) but the iterations can separate them clearly (for an example see Figure 7).

It is necessary to note that the estimated radiant point of the SF component and FTA coincides perfectly;

Table 4d – Estimated elements of FTA.

λ_s	$\lambda-\lambda_s$	β	α	δ	V_g	e	q	i	ω	Ω	λ_Π	β_Π	a
230	187.9	−4.9	56.8	14.9	24.4	0.760	0.453	4.5	104.9	50.0	154.9	4.3	1.88
235	186.3	−5.5	60.3	15.0	23.8	0.753	0.480	4.8	101.4	55.0	156.4	4.7	1.94
240	184.7	−6.1	63.9	15.0	23.3	0.747	0.507	5.0	97.9	60.0	158.0	5.0	2.00
245	183.1	−6.7	67.5	15.0	22.7	0.742	0.534	5.3	94.5	65.0	159.5	5.2	2.06
250	181.5	−7.3	71.0	14.9	22.1	0.736	0.560	5.5	91.1	70.0	161.1	5.5	2.12
255	179.9	−7.9	74.5	14.7	21.6	0.731	0.585	5.6	87.8	75.0	162.8	5.6	2.18
260	178.3	−8.5	78.1	14.4	21.0	0.726	0.610	5.8	84.5	80.0	164.5	5.7	2.23

Table 4e – Estimated elements of NTA.

λ_s	$\lambda-\lambda_s$	β	α	δ	V_g	e	q	i	ω	Ω	λ_Π	β_Π	a
200	199.4	2.0	36.3	16.5	32.0	0.883	0.222	3.3	311.1	200.0	151.2	−2.5	1.90
205	198.0	2.0	39.9	17.7	31.2	0.873	0.245	3.2	308.1	205.0	153.1	−2.5	1.93
210	196.7	2.1	43.6	18.9	30.5	0.863	0.270	3.1	305.0	210.0	155.1	−2.5	1.96
215	195.4	2.2	47.3	20.0	29.8	0.852	0.294	3.0	302.0	215.0	157.0	−2.5	1.99
220	194.1	2.3	51.1	21.0	29.0	0.842	0.319	2.9	299.0	220.0	159.0	−2.5	2.01
225	192.7	2.4	54.9	22.0	28.3	0.831	0.344	2.8	296.0	225.0	161.0	−2.5	2.04
230	191.4	2.4	58.7	22.8	27.6	0.820	0.370	2.7	293.0	230.0	163.0	−2.5	2.06
235	190.1	2.5	62.6	23.6	26.8	0.809	0.395	2.6	290.0	235.0	165.0	−2.5	2.07
240	188.8	2.6	66.6	24.3	26.1	0.798	0.421	2.6	287.1	240.0	167.1	−2.5	2.08
245	187.4	2.7	70.6	24.9	25.4	0.787	0.446	2.5	284.1	245.0	169.2	−2.4	2.09
250	186.1	2.7	74.6	25.4	24.6	0.775	0.471	2.4	281.3	250.0	171.3	−2.4	2.10
255	184.8	2.8	78.6	25.8	23.9	0.763	0.496	2.4	278.4	255.0	173.4	−2.3	2.10
260	183.4	2.9	82.7	26.1	23.2	0.751	0.521	2.3	275.6	260.0	175.6	−2.3	2.09

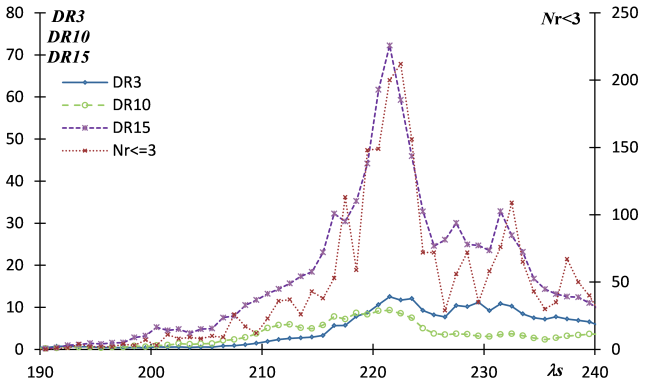

Figure 10 – Activity profile of SF component; see Section 2.2 for the explanation of Nr ≤ 3, DR3, DR10 and DR15.

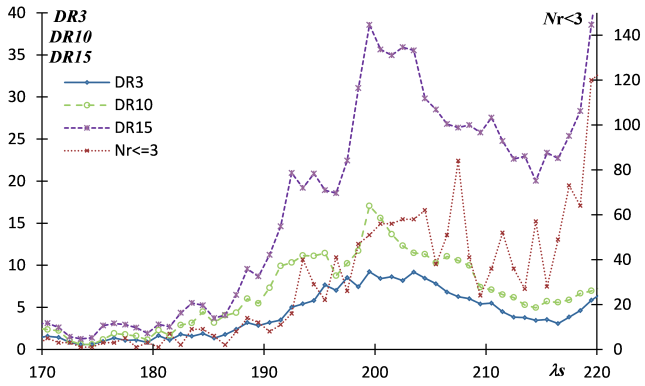

Figure 11 – Activity profile of SE component.

$(\lambda-\lambda_s, \beta) = (186.3, -5.5)$ at $\lambda_s = 235°$. We get clearer evidence to unite the SF component and FTA.

3.2 Activity profile

Figures 10–14 give the activity profiles counting meteors along with the estimated radiant point. It is necessary to stress that DRs are the relative intensity of each shower activity to the sporadic background and the results cannot be compared with other showers directly.

Figure 10 proves the smooth activity change of the SF component and the change is rapid contrary to the usual belief; the full width at half maximum seems to be less than a week, not over a month. It should be stressed that Southern Taurids have two components SE and SF and they are clearly independent.

The activity profile of SE (Figure 11) is affected by SF after $\lambda_s > 210°$ largely because we do not exclude SF candidate meteors in this figure; SF catches up after $\lambda_s = 210°$ (see Section 3.1). It is proper to name this activity as 'Southern Arietids' or 'Nighttime Arietids' but not 'Southern Taurids'; SE activity is clearly independent and its radiant point is located in Aries at the maximum (around $\lambda_s = 200°$).

The activity profiles of ORS (Figure 12) and FTA (Figure 13) might be represented by DR3 not DR15 in these cases because they are active around $\lambda_s = 250°$ when #250NOO and #019MON influence the background meteors. But, if the maximum of FTA occurred before $\lambda_s < 240°$, the influences can be ignored and DR15 could show the useful information; the maximum of FTA would be coincident with the SF component around $\lambda_s = 220°$, suggesting they could be united.

NTA activity (Figure 14) is represented by DR15 but the dip around $\lambda_s = 225°$ creates a false second peak before the main maximum. Perhaps, this dip is resulting from the observational conditions; DR15 of the

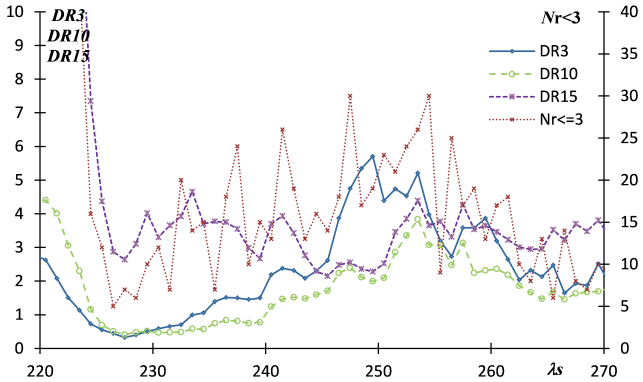

Figure 12 – Activity profile of ORS.

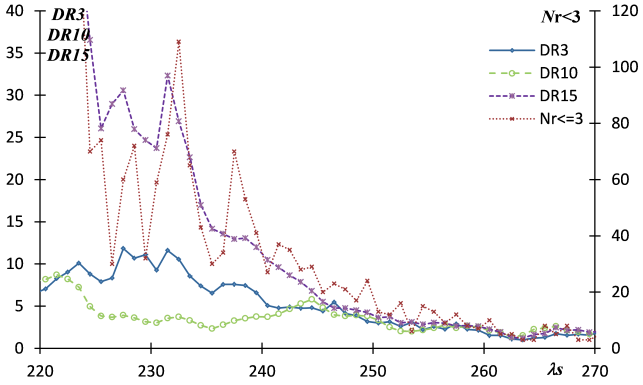

Figure 13 – Activity profile of FTA.

SF component is affected by this problem as discussed below (see last paragraph of Section 4).

4 Discussion

We cannot find any signs of 'mini' or related showers both in radiant distributions (Figures 5–9, see also all the panels of Figure 17, from $\lambda_s = 180$ to 270°) and activity profiles (Figures 10–14). There are three components – SE, SF and NTA – though some would intend to include ORS in 'Taurids'.

Asher & Clube (1993) suggested the Taurids have a swarm of meteoroids locked in 7:2 resonance with Jupiter and Asher & Izumi (1998) confirmed the existence of the swarm by visual observations. Table 5 shows clearly the SF component gave an enhanced activity in 2015 and the other 4 components did not. Shiba (2016) and Spurný et al. (2017) reported 2015 enhanced activity and the enhancement was caused by a swarm of meteoroids locked in 7:2 resonance with Jupiter. Spurný et al. (2017) called the responsible activity a 'new branch' of the Southern Taurids but this is the SF component. Koseki (2012a) selected 40 photographic SF meteors and Table 6 lists their distribution by observational years. Super Schmidt cameras naturally caught many SF meteors in 1953, 1956 and 1958, but it is notable that small cameras which could not photograph faint meteors recorded the enhanced activity in 1937 and 1964.

The activity profiles of the enhanced years, 2008, 2012 and 2015, are sharper than Figure 10 and those of the average years are gentle. The activity of the SE

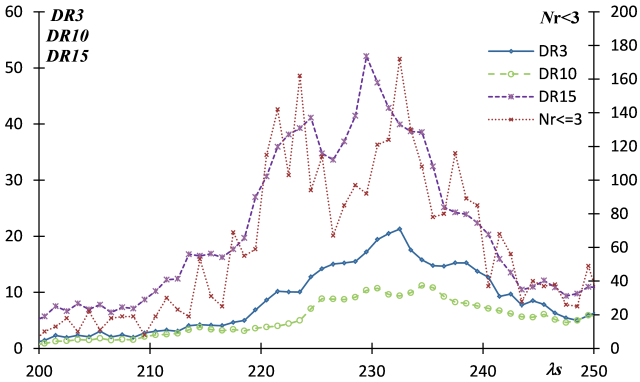

Figure 14 – Activity profile of NTA.

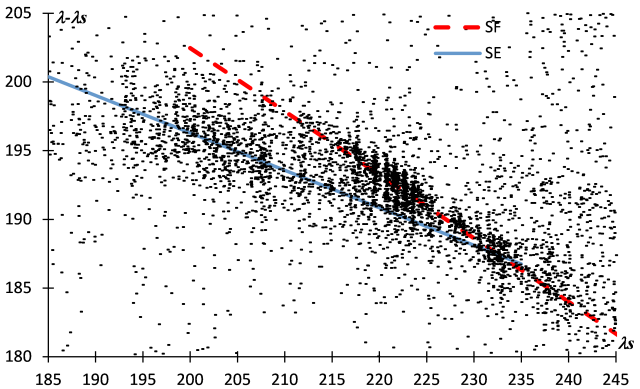

Figure 15 – The distribution of radiants $180 < \lambda - \lambda_s < 205$, $-8 < \beta < -2$, between $185 < \lambda_s < 245$. It is clear there are two components; fast moving SF (broken line) and slow SE (solid line).

component is comparable to that of SF in the average years and, therefore, it is natural to unite them and to think 'Taurids are active over two months'. Figure 15 clearly shows 'Southern Taurids' consist of two components: SE and SF. The SF component is locked in 7:2 resonance with Jupiter and not part of the general 'Southern Taurids' including the SE component.

We can estimate the activity profile of the SF component using the method presented by Koseki (2012b) because its perihelion is stationary. Figure 16 shows the estimation with the observational results and they are in good agreement; the discrepancy in the last stage

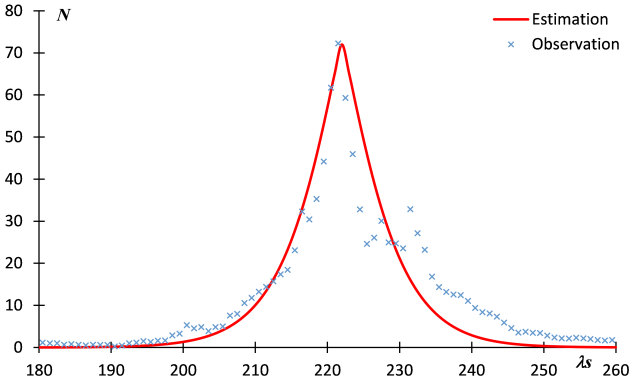

Figure 16 – Comparison of DR15 profile of SF component (crosses) with the estimation of the activity calculated from the orbit (Koseki, 2012b).

Table 5 – Selected meteors by the condition of Table 3.

Year	2007	2008	2009	2010	2011	2012	2013	2014	2015	2016	2017	2018
SF	17	170	43	40	27	160	31	12	359	31	48	94
SE	13	54	91	26	17	80	42	50	61	52	8	37
ORS	8	24	15	26	11	9	29	9	13	14	18	15
FTA	15	50	26	19	37	35	23	17	30	19	35	56
NTA	178	202	273	291	196	272	217	250	163	237	334	303

Table 6 – Photographic SF meteors; predicted enhanced years are in bold.

Year	**1937**	**1947**	1950	1952	1953	**1954**	1956	1958	1959	**1961**	1962	**1964**	1974	Total
N	4	1	1	3	7	1	5	7	1	1	1	7	1	40

might be related to FTA (see next paragraph). We recognize the DR15 curve is the most suitable expression of the SF activity profile, because NTA is present within 10° and the outskirts of the SF component still exist within 6° after the iterations.

The radiant distributions of SF and SE components project into the radiant region of each other (Figures 5 and 6); the left side of SE seems the precursor of SF and right side of SF the remnant of SE or early FTA activity. It is very interesting that the estimated radiants of SE, SF and FTA are located at almost the same position between $230 < \lambda_s < 235$ (Tables 4a, 4b and 4d), though the estimated activity of SE has ceased then. Does 'FTA' start its activity long before listed in the SD and reach its maximum between $230 < \lambda_s < 235$? Does the SF component have the secondary peak around $230 < \lambda_s < 235$? These questions are too difficult to answer even using SonotaCo net's abundant data and still remain unknown.

We can detect ORS as a weak independent activity but ORN is not perceptible (255, 260 and 265 of Figure 17). The unreasonable belief that there could be southern and northern branches in the ecliptic showers usually still remains.

The dips of the activity profiles of the SF component and NTA are caused by the insufficient number of observations. The weather conditions obstructed observations in 2015; only one meteor was recorded between $223.87 < \lambda_s < 226.87$. We should be careful when studying meteor shower activities; raw observational data are not uniformly distributed.

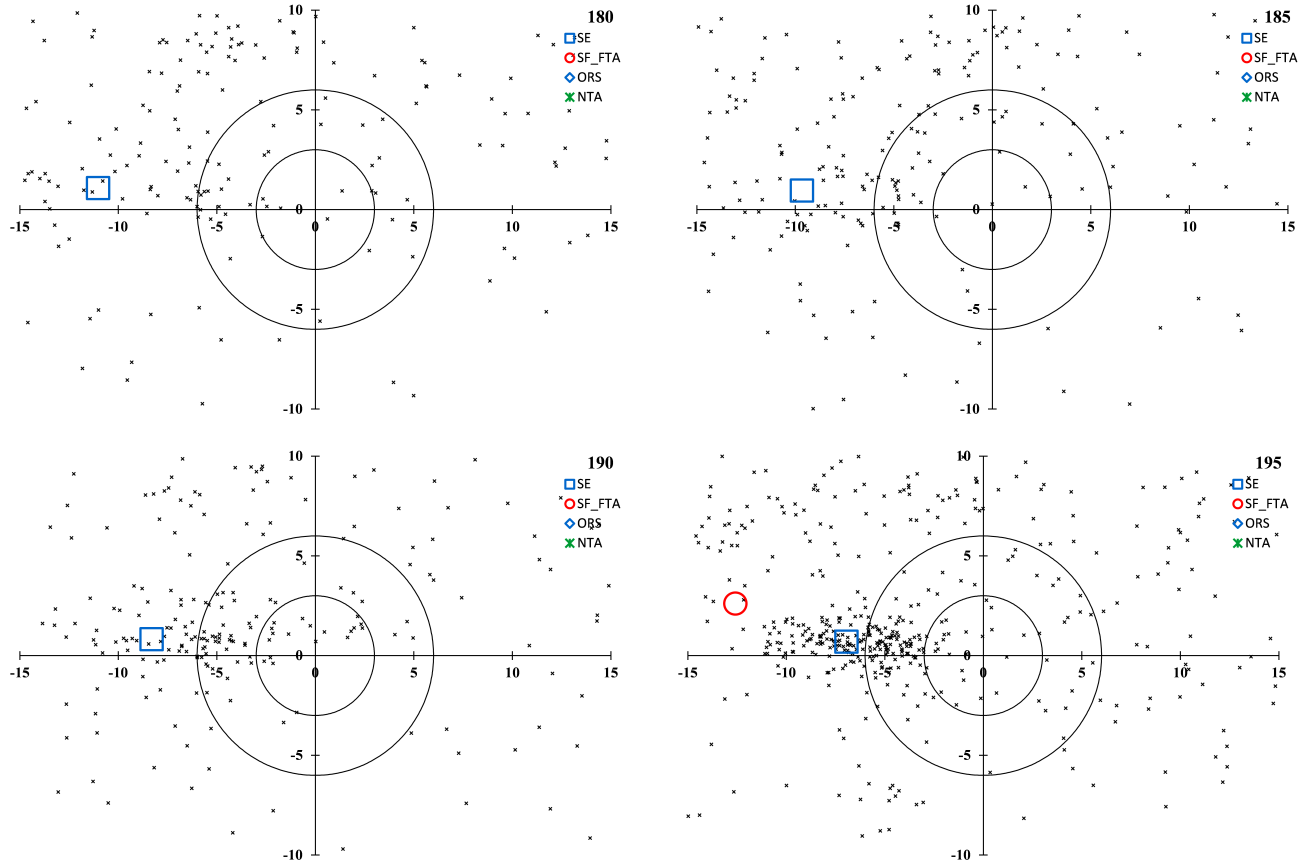

Figure 17 – Radiant distributions of video meteors. The numbers at the top right are the midpoint of the λ_s range, the range covering ±2.5 degrees from the midpoint; e.g., the figure 180 includes radiants between $177.5 < \lambda_s < 182.5$.

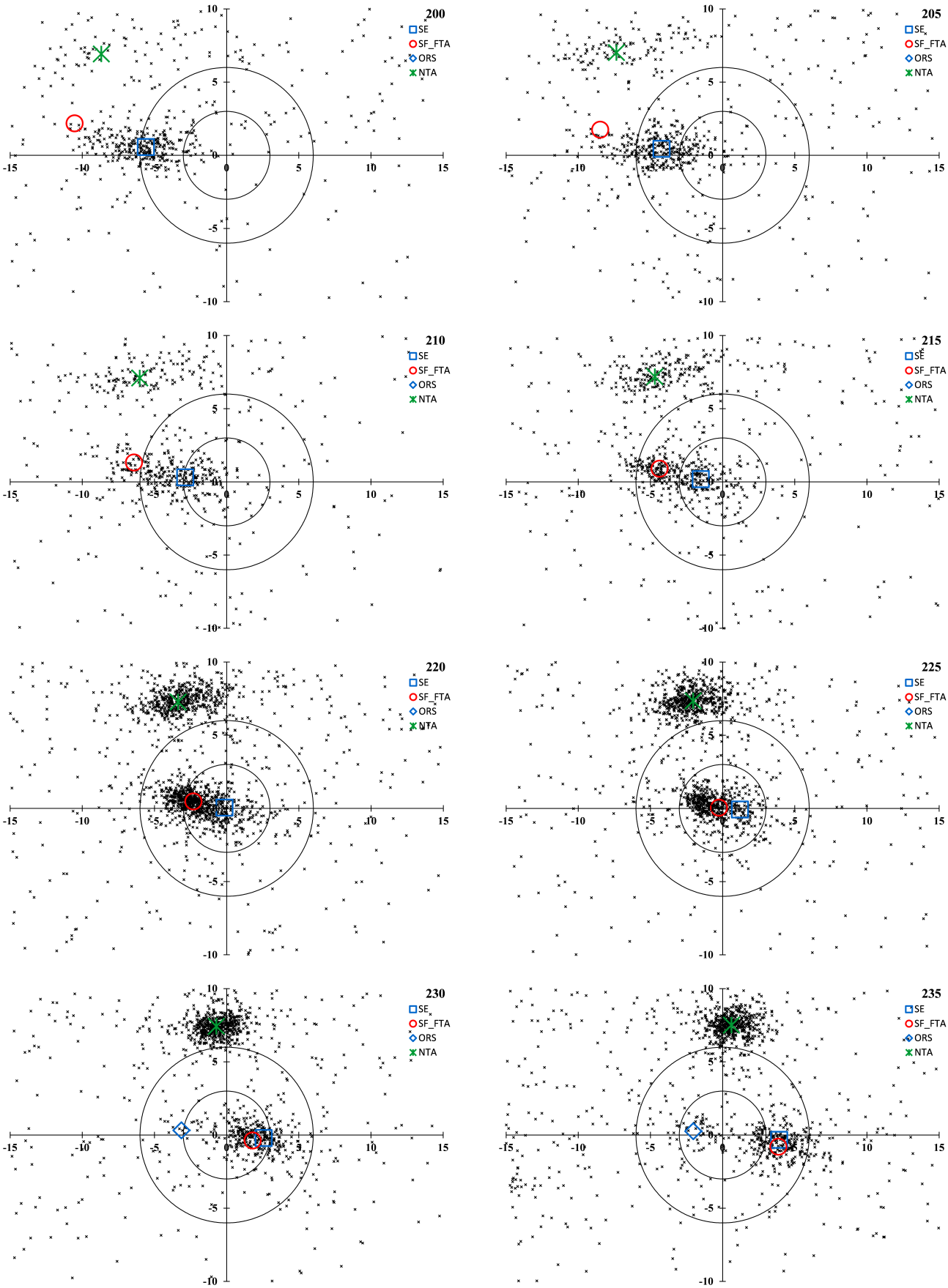

Figure 17 – continued from previous page.

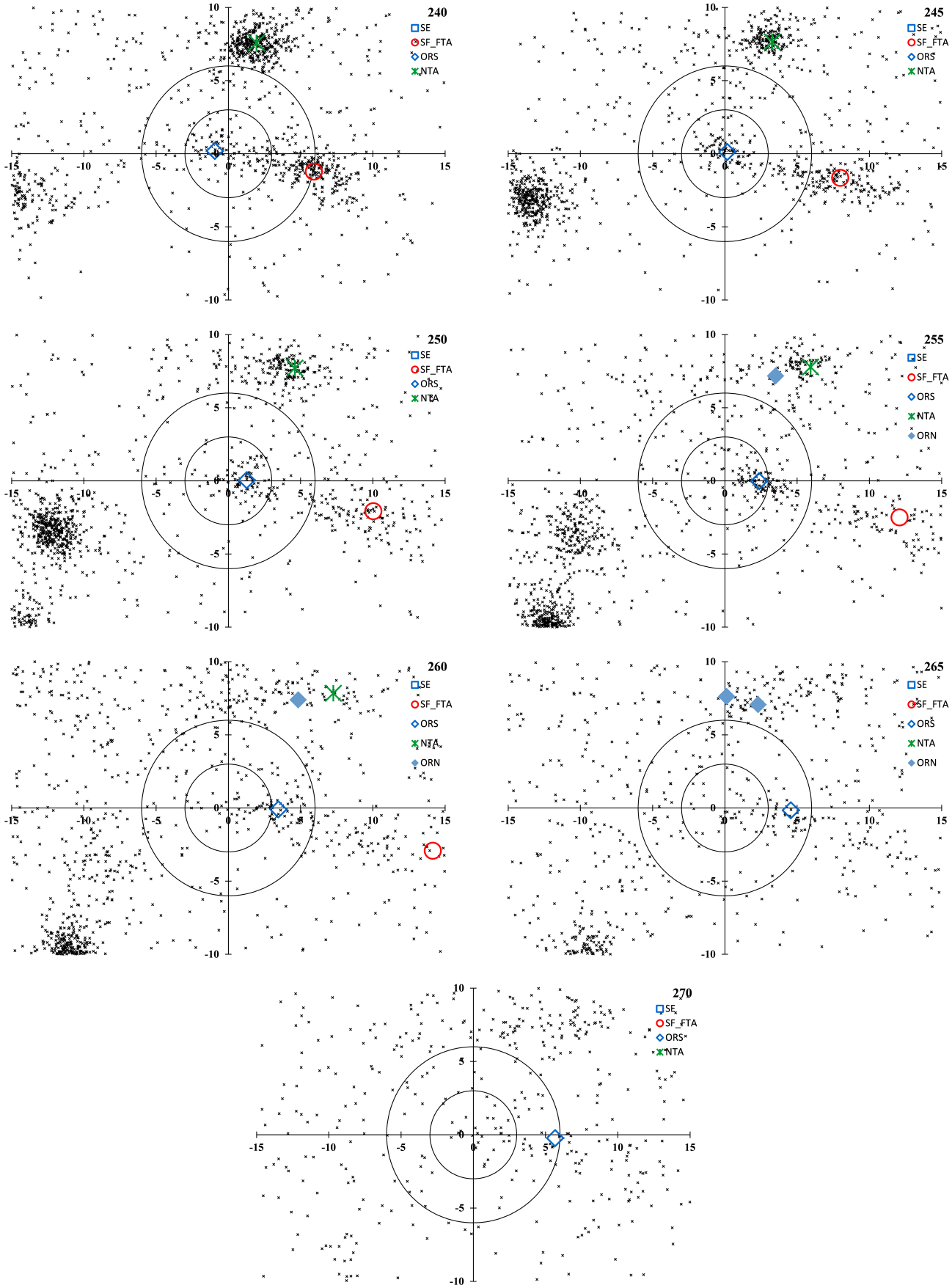

Figure 17 – continued from previous page.

5 Conclusions

We can confirm two unique components in 'Southern Taurids': SE (Steady Expression of Southern Arietids) and SF (Sharply Fluctuating component of 'Southern Taurids'). 11 years almost uniform observations of the SonotaCo network permit us to show the enhanced activity of the SF component in the predicted years (Asher & Clube, 1993) clearly.

It could be suggestive to future investigations that the estimated radiants of SE, SF and FTA are located at almost the same position between $230 < \lambda_s < 235$. The SF component and FTA might be one shower but the SE component seems to be independent. Whether this coincidence is by chance, and the origin of the three, remain to be studied.

ORS and NTA are both independent activities; we had better reject the old idea that there should commonly exist both southern and northern branches in ANT activities.

References

Asher D. J. and Clube S. V. M. (1993). "An extraterrestrial influence during the current glacial-interglacial". *Quarterly Journal R. Astron. Soc.*, **34**, 481–511. See also "Taurid swarm years", `http://www.cantab.net/users/davidasher/taurid/swarmyears.html`.

Asher D. J. and Izumi K. (1998). "Meteor observations in Japan: new implications for a Taurid meteoroid swarm". *Mon. Not. R. Astron. Soc.*, **297**, 23–27.

Koseki M. (2012a). "Three components of 'Taurids'". *WGN, Journal of the IMO*, **40:4**, 129–138.

Koseki M. (2012b). "A simple model of spatial structure of meteoroid streams". *WGN, Journal of the IMO*, **40:5**, 162–165.

Koseki M. (2019). "Profiles of meteor shower activities inferred from the radiant Density Ratios (DR)". *WGN, Journal of the IMO*, **47:6**, 168–179.

Shiba Y. (2016). "Taurid swarm exists only in southern branch (STA)". *WGN, Journal of the IMO*, **44:3**, 78–91.

SonotaCo (2009). "A meteor shower catalog based on video observations in 2007–2008". *WGN, Journal of the IMO*, **37:2**, 55–62. See also "SonotaCo Network Simultaneously Observed Meteor Data Sets", `http://sonotaco.jp/doc/SNM/`.

Spurný P., Borovička J., Mucke H., and Svoreň J. (2017). "Discovery of a new branch of the Taurid meteoroid stream as a real source of potentially hazardous bodies". *Astron. Astrophys.*, **605**, A68.

Handling Editor: David Asher

A brief pre-maximum peak in the Quadrantids 2020

Jürgen Rendtel [1], *Hirofumi Sugimoto* [2]

The main maximum of the visual Quadrantids occurs annually with very little variation at $\lambda_\odot = 283\,^\circ\!.15 \pm 0\,^\circ\!.04$. In 2020 this position was reached on January 4 near 08^hUT, thus favourable for North American longitudes. Observations of the ascending branch showed a short peak at $\lambda_\odot = 282\,^\circ\!.880$ (2020 January 4, 02^h UT). This peak is found in visual and radio forward scatter data. The position and duration perfectly coincides with a pre-maximum peak observed in 2016. Analyses of data from the period 2004 – 2020 show similar peaks in 2008, 2009, 2014, 2016 and 2020. The 2008, 2016 and 2020 peaks occurred very close to $\lambda_\odot = 282\,^\circ\!.880$ within $\pm 0\,^\circ\!.02$, while the 2009 and 2014 peaks are $0\,^\circ\!.4$ and $0\,^\circ\!.08$ earlier, respectively. Further, we summarize the Quadrantid main maximum ZHR and positions for the period 2004 – 2020.

Received 2020 May 1

1 Introduction

The Quadrantids is one of the attractive meteor showers for visual observers in the northern hemisphere. For a short period it produces high rates. Although the level varies from one return to the next, we find ZHR $\approx 90 - 120$. The position of the peak is regularly found close to $\lambda_\odot = 283\,^\circ\!.15 \pm 0\,^\circ\!.04$, and the typical width of the peak (FWHM) is of the order of 4 hours. Therefore, each annual return favours a limited longitude range of the globe where the radiant is well above the horizon within the dark night. At 55° N, this covers about six hours, and is less for more southern locations and essentially more than 14 hours for latitudes north of 60°.

In 2020 the above given position was reached on January 4, 08^h UT – optimal for North American locations. Weather permitting, observers in Europe had the chance to follow the ascent until dawn, terminated by twilight. Via the IMO web page, we received a reasonable amount of visual Quadrantid data which are analysed here.

Other data have been collected by video camera systems spread over a larger region and by radio forward scatter systems. The data can be accessed on the FluxViewer webpage and the radio ZHR page of Sugimoto (`http://www5f.biglobe.ne.jp/~hro/Flash/2020/QUA/index.html`).

2 Data of the 2020 return

For this study we used visual, video and radio forward scatter data collected by observers worldwide. The graphs shown here consider data available by April 27 (visual, video) and April 4 (radio).

Visual data have been submitted to the IMO's VMDB by 26 observers: Pierre Bader, Felix Bettonvil, Kolyo Dankov, Michel Deconinck, Howard Edin, Kai Gaarder, Christoph Gerber, Hansub Jung, Javor Kac, Robert Lunsford, Pierre Martin, Frederic Merlin, Francisco Ocaña González, Lovro Pavletić, Ina Rendtel, Jürgen Rendtel, Terrence Ross, Branislav Savic, Alex Scholten, Kai Schultze, Ivan Sergey, Ulrich Sperberg, Shigeo Uchiyama, Hendrik Vandenbruaene, Roland Winkler, Sabine Wächter. The resulting general ZHR profile for the entire Quadrantid return from end December 2019 into January 2020 is shown in Figure 1.

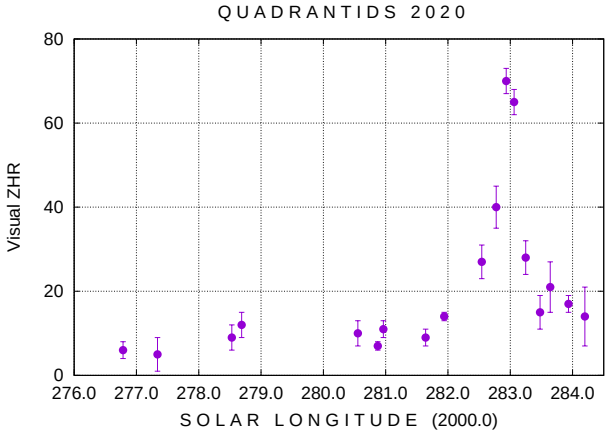

Figure 1 – Visual Quadrantid ZHR of the 2020 return (population index applied $r = 2.10$ for the entire period).

For the **video data** analysis we used the temporary data base which is accessible via the meteoflux webpage `https://meteorflux.org/` (access date as indicated in the Figure caption). Throughout the paper we shorten flux density into flux.

Radio forward scatter data of the following contributing stations have been included in the calculation of the ZHR_r: Josephco _@_IEPER, Chris Steyaert (Belgium), ASU-R0, FLZ-R0, OBSUPICE-R6, VALMEZ-R1 (Czech Republic), Halei Test (China), Jean Marie F5CMQ, DanielD SAT01_DD (France), Per DL0SHF, WHS Essen (Germany), Mario Bombardini, Fabio Moschini_IN3GOO (Italy), Kenji Fujito, Kazuyoshi Kanatsu, Nobuo Katsura, Naoya Saito, Hironobu Shida, Tosihide Sowa, Hirofumi Sugimoto, Masaki Tsuboi (Japan), Meteorkees (The Netherlands), Simon Holbeche, Philip Norton, Philip NortonVert, James Screech, Bill Ward (United Kingdom).

The 2020 ZHR profile from the visual data has its maximum significantly earlier than the average peak time observed in most years: the reference position of

[1] Leibniz-Institut für Astrophysik, An der Sternwarte 16, 14480 Potsdam, Germany
and International Meteor Organization, Eschenweg 16, 14476 Potsdam, Germany.
Email: `jrendtel@web.de`
[2] Nippon Meteor Society, Japan.
Email: `sugimoto.hro@gmail.com`

IMO bibcode WGN-482-rendtel-qua
NASA-ADS bibcode 2020JIMO...48...47R

the main maximum is at $\lambda_\odot = 283\,^\circ\!.15 \pm 0\,^\circ\!.04$. The visual peak ZHR of the 2020 return is in the lower range of the observed values over the past decades (Table 1). Variations of the peak time and the maximum ZHR have been found also in previous years, although in several cases it must remain open whether this is a true density variation in the stream or a bias due to the limited observing possibilities. The shower can be observed for only about 6 hours per night (Table 2) from mid to far northern latitudes and has further limitations because of moonlight and often poor weather conditions over large regions.

3 Ascent to the Quadrantid maximum 2020

Most observers aim at the main Quadrantid maximum with attractive rates and bright meteors. The short duration of the peak implies that we should have a reasonable number of reports concerning both slopes of the profile. It seems that most analyses also concentrated to the central section of the stream. Results describe the difference in the (slower) ascent towards and the (steeper) descent after the peak. By now we had no indication of an activity variation in the ascent towards the main maximum. Details are described and illustrated for the "best observed" 1992 return. The profile of the ascending branch is smooth (with little variations only, and all of these well within the error margins – see Figure 4 in Rendtel, Koschack & Arlt, 1993).

In 2020, the main peak was expected to occur in the European daytime (8^hUT) and thus too early for many North American observers. Therefore the ascending branch is well covered by visual observers from European longitudes (Figure 2) and the later descent from North American locations. During the ascent we find a short increase of the ZHR. This was very obvious and has been described by observers like "for about 20–30 minutes the shower left the impression of a major shower peak with a high cadence of meteors, among these numerous bright Quadrantids, which stopped abruptedly."

A similar short-lived and significant increase is found in the radio forward scatter data. The derived radio-ZHR is also plotted in Figure 2. Surprisingly, the temporary video data do not show an increase at the same position (lower data points in Figure 2).

This short peak is only represented by a few intervals with a high ZHR. However, the ZHR (both in visual and radio data) exceeds the level of the neighbouring values by more than the size of the error margins. Some observers noticed similarities to the 2016 Quadrantid return. Hence we looked into the same section of the profile in previous years.

4 Ascending branch in other years

As already mentioned, the well analysed 1992 return had no such feature in the ascending branch of the rate profile. Next, we checked all other, more recent returns in the period 2004 to 2020. Back in 2016, a possible peak well before the main maximum was announced. In the IMO Meteor Shower Calendar 2016 (Rendtel, 2015) it is stated, that "model calculations of Vaubaillon provide indications that the peak may occur earlier and may show a maximum between January 3, 22h, and January 4, 2h UT". While the main maximum did not occur earlier in 2016 (Table 1), a pre-maximum peak was found in the data (Rendtel et al., 2016). For 2020, there was no prediction of increased activity.

The results for the ascending branch of the annual returns are summarized below. Years which show peculiarities in the ascending branch profiles are set in bold.

Visual:

2004: two ZHR points at $282\,^\circ\!.672$ (92 ± 13) and $282\,^\circ\!.706$ (86 ± 12) i.e. Jan 03, 18:36/19:25 (mainly Japanese observers), no data point before $282\,^\circ\!.67$
2005: no profile
2006: Jan 03, 17:01 $283\,^\circ\!.105$ local peak, but only 2 intervals (37 QUA; ZHR 98 ± 16)
2007: no profile
2008: Jan 03, 23:56 $282\,^\circ\!.874$ local peak, 3 intervals (50 QUA; ZHR 71 ± 10)
2009: Jan 03, 05:20 $282\,^\circ\!.843$ steady increase, later decrease (FWHM rather 4 hours!); peak value 23 intervals (356 QUA; ZHR 107 ± 6)
2010: too few points
2011: too few points
2012: smooth ascent until $283\,^\circ\!.0$
2013: ascent not observed
2014: no data $282\,^\circ\!.9$ – $283\,^\circ\!.1$ but local maximum as early as Jan 03, 10:59, $282\,^\circ\!.793$, only 2 intervals (23 QUA; ZHR 82 ± 17)
2015: too few points
2016: Jan 04, 01:38, $282\,^\circ\!.892$, 5 intervals (47 QUA; ZHR 67 ± 10)
2017: Jan 03, 06:38, $282\,^\circ\!.842$, only 3 intervals (19 QUA; ZHR 98 ± 22), main maximum not well established, hence early peak doubtful
2018: no data $282\,^\circ\!.7$ – $283\,^\circ\!.3$
2019: ascent not observed, no data $282\,^\circ\!.2$–$283\,^\circ\!.0$
2020: pre-maximum peak (this work)

We analysed visual data of 17 Quadrantid returns to check for similar pre-maximum ZHR peaks. Eight of the profiles did not cover the ascending branch sufficiently. Five of the remaining nine profiles show a peak close to the 2020 and 2016 timings (Figure 3). Of these, the 2009 local maximum occurs in the general ascent (also with a generally higher ZHR level) and is not as pronounced as the others. So there are four clear occurrences of a peak in the years 2008, 2014, 2016 and 2020. The position in solar longitude of the 2008, 2016 and 2020 pre-maximum peaks is very close to each other in varies only by less than half an hour (about $0\,^\circ\!.02$), while the 2014 peak is about 2 hours earlier.

Radio:

2011, 2012, 2013, 2018, 2019 no pre-maximum peak
2014 shoulder at $282\,^\circ\!.8$ (80 ± 5), fits the visual peak position (cf. Figure 3)

Table 1 – **Quadrantid main maximum data** in the period 2004 – 2020 derived from visual data. Video and radio forward scatter data are available from 2012 onwards. **Visual:** since we look for the general peak level, we used bin width of 1–2 hours and $r = 2.10$. (Int, QUA – number of intervals/Quadrantid meteors defining the peak value.) **Radio:** The 2016 ZHR_r maximum is broad between 283.°15–283.°35. **Video:** 2017 – only one single value at 283.°11 32.3 ± 6.4; 2018 – broad maximum.

Year	Jan	UT	$\lambda_\odot$	Int	QUA	ZHR	err	$\lambda_\odot$	ZHR_r	err	$\lambda_\odot$	Flux	err
		Visual data						Radio data			Video data		
2004	03	23:13	282.868	7	55	102	14						
2005	03	23:13	283.295	5	74	55	6						
2006	03	21:13	283.283	8	29	74	14						
2007	04	few data only before the peak											
2008	04	08:49	283.252	50	188	82	6						
2009	03	10:17	283.053	47	769	153	6						
2010	03	18:34	283.138	4	16	75	18						
2011	03	22:01	283.029	30	209	84	6						
2012	04	05:08	283.067	51	416	72	4	283.1	135	10	283.304	24.2	3.4
2013	03	12:44	283.130	10	101	80	8	283.3	105	7	peak not covered		
2014	03	18:08	283.097	14	85	106	11	283.2	115	7	283.057	47.9	5.4
2015	03	23:00	283.304	214	1742	94	2	283.3	75	10	283.163	11.2	1.0
2016	04	09:32	283.227	13	132	91	8	283.25	140	10	283.2	23.1	4.6
2017	03	10:31	283.006	4	80	75	8	283.25	115	10	283.11	32.3	6.4
2018	03	no near peak data						283.25	108	25	283.3	10.8	1.5
2019	04	01:57	283.142	89	769	107	4	283.18	125	10	283.146	22.8	0.7
2020	04	04:27	282.986	47	414	79	4	283.15	128	15	282.868	17.1	1.0

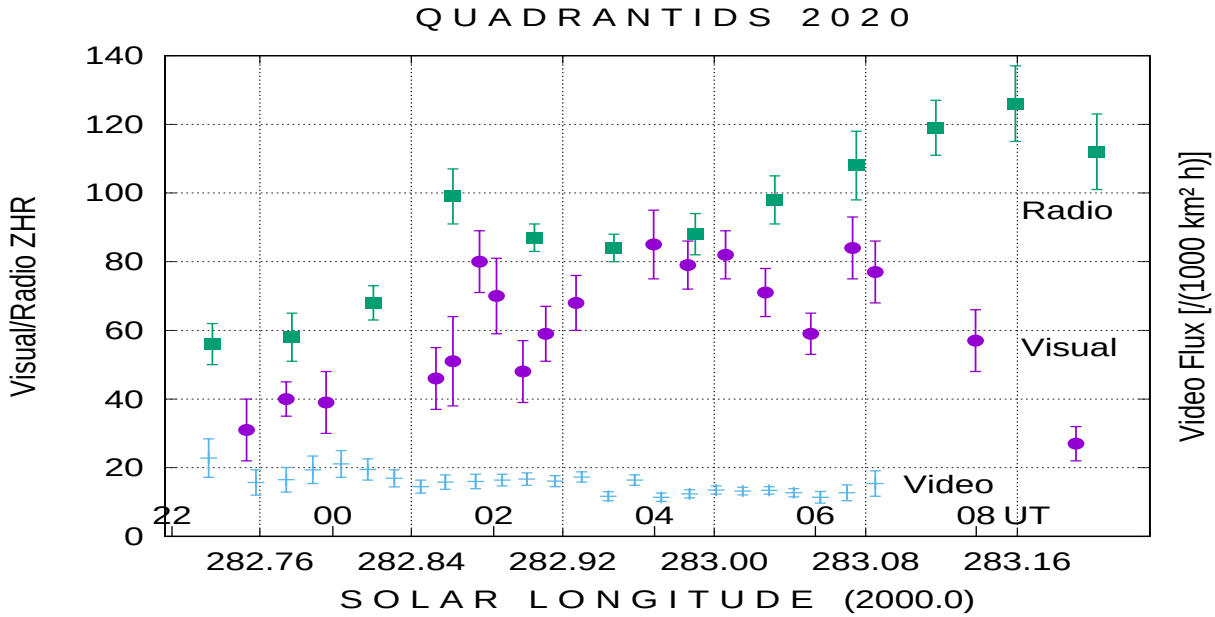

Figure 2 – Quadrantid activity on 2020 January 3/4 derived from visual, radio forward scatter data (left scale) and video data (right side scale) during the ascent towards the main maximum. Data extracted as of 2020 April 27 (visual and temporary video) and 2020 April 04 (radio forward scatter).

2015 very weak single point 282.°88 (50 ± 5) – less than error bar size
2016 sharp peak 282.°75 (88 ± 5) – part of the 2016 analysis
2017 maximum at 283.°0 (95 ± 5) = yes
2020 pre-peak at 282.°85 (88 ± 10) = yes; this work

Radio data confirm the 2014, 2016 and 2020 peaks. There is also a peak in the 2017 profile. In this case, the visual profile does not allow us to confirm the structure.

Video:
2012, 2013, 2014 no pre-peak
2015 no profile
2016: pre-peak 282.°888 (15.9 ± 1.3 – 2016 analysis)
2019: pre-peak 282.°887 (16.7 ± 2.8) single prominent point
2020 ascending branch with large gap (preliminary data only)

Video flux density peaks are found in 2016 and 2019.

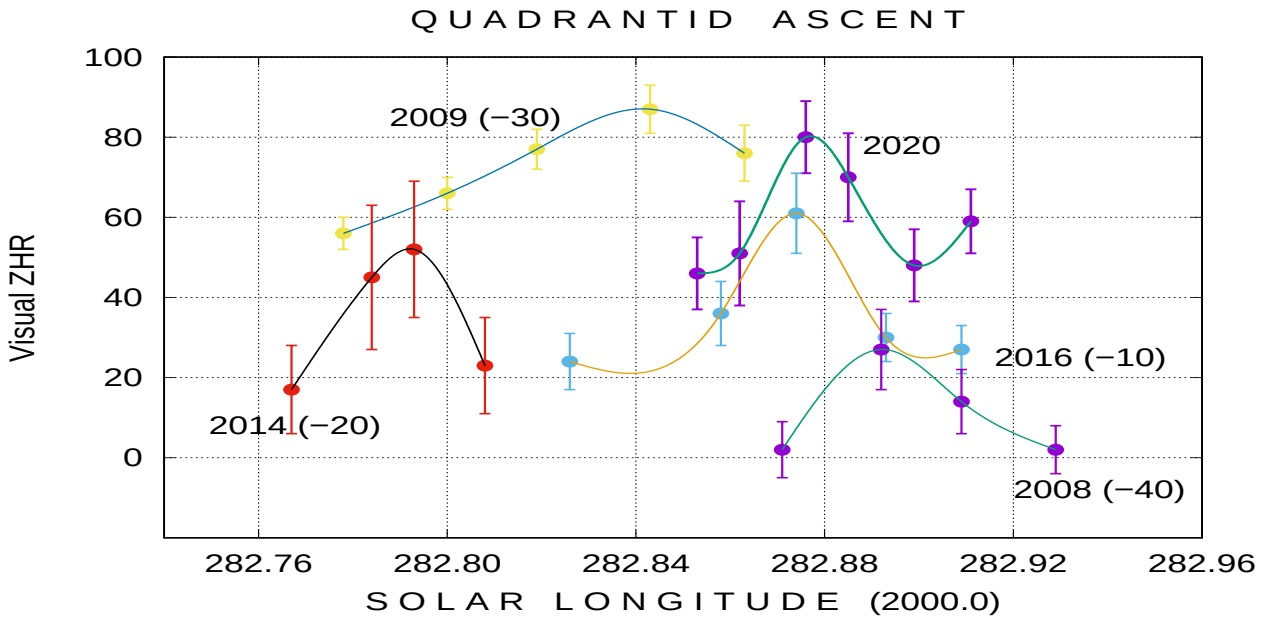

Figure 3 – Visually observed Quadrantid activity of the ascending branch in the years which show short lived ZHR peaks. The ZHR level has been shifted as indicated in the labels to avoid overlapping of the profiles. The profile lines shown are a spline fit to connect the individual points. The 2008, 2016 and 2020 peaks occurred at the same position ($282\overset{\circ}{.}88 \pm 0\overset{\circ}{.}02$). $0\overset{\circ}{.}04$ correspond to about 1 hour; the main Quadrantid maximum is close to $283\overset{\circ}{.}15$.

Table 2 – Timing of the average **main peak position** at $\lambda_\odot = 283\overset{\circ}{.}15$ (nearest hour); the pre-maximum position which discussed here near $\lambda_\odot = 282\overset{\circ}{.}9$ is reached about 6 hours earlier. The period 14^h–20^h UT coincides with the "Pacific gap" from which almost no observations of the far northern Quadrantids are available.

Year and date	Peak (UT)	Radiant high in the sky
2004-01-04	06^h	W Europe – E North America
2005-01-03	12^h	North America
2006-01-03	18^h	Pacific
2007-01-04	00^h	Asia – E Europe
2008-01-04	06^h	W Europe – E North America
2009-01-03	13^h	North America
2010-01-03	19^h	Pacific
2011-01-04	01^h	W Asia – E Europe
2012-01-04	07^h	W Europe
2013-01-03	13^h	North America
2014-01-03	19^h	Pacific
2015-01-04	02^h	W Asia – E Europe
2016-01-04	08^h	W Europe – E North America
2017-01-03	14^h	North America
2018-01-03	20^h	Pacific – E Asia
2019-01-04	02^h	W Asia – E Europe
2020-01-04	08^h	West Europe

5 Conclusions

We find a short-lived peak in the ascending branch of the Quadrantids at a four occasions in the period 2004–2020, observed in 2008, 2014, 2016 and 2020. For the 2009 and 2017 returns, the data is not conclusive.

For geometrical reasons, the observations in leap years are favourable as there are many visual observers in the region with high radiant position in the second half of the local night, while particularly the radio data provide a continuous data set. However, the observed pre-maximum peaks are not restricted to these geometric favourable conditions.

The first reported peak was found in 2016, confirming a prediction based on meteoroid stream modelling. In 2020, there was no prediction of any activity peculiarity. We suggest to check whether models may provide hints at further density increases.

The evolution of the high inclination Quadrantid stream seems to be difficult to model, partly because there is no reference period for particle releases from one of the parents 2003 EH_1 and 96P/Machholz. Currently, we cannot say anything about the duration over which such a feature like the peak can be detected. Perhaps the events help to access the question whether we see a short-lived structure in the stream or traces of an extended feature.

References

Rendtel J. (2015). "2016 Meteor Shower Calendar". International Meteor Organization. IMO_INFO (2-15), pages 4–5.

Rendtel J., Koschack R., and Arlt R. (1993). "The 1992 Quadrantid meteor shower". *WGN, Journal of the IMO*, **21**, 97–109.

Rendtel J., Ogawa H., and Sugimoto H. (2016). "Quadrantids 2016: observations of a short pre-maximum peak". *WGN, Journal of the IMO*, **44**, 101–107.

Handling Editor: Javor Kac
This paper has been typeset from a LaTeX file prepared by the authors.

Radar meteors

Distribution of sporadic meteor background from 40-years old radar observations

Peter Zimnikoval[1,2], *Daniel Očenáš*[1], *Miroslav Znášik*[1,3], *Juraj Škvarka*[1,4], *Ján Fabricius*[1], *Stanislav Kaniansky*[5]

An extensive project involving the observation by radar of sporadic meteors was carried out at Ondřejov, Czech Republic during the years 1981 to 1983. Until now, the observational data collected had not been evaluated – only a quantitative review had been published (Fabricius, Kaniansky & Škvarka, 1993). After almost 40 years, I found this forgotten data from radar observations while preparing a historical review for a memorial to 60th anniversary of the Observatory in Banská Bystrica, Slovakia. Together with my former colleagues, I had active participation on the project. The data is primarily in a digital format. Using the contemporary facilities of computers, I have made an attempt to evaluate it. A graphical method for distribution of probable radiant positions was used.

Received 2020 February 28

1 Observation

Meteor radar at Ondřejov, at that time the Czechoslovak Meteor Radar, was an old aviation instrument, accommodated for meteor research (Figure 1). It was used for the monitoring of the activity of main meteor showers by both Czech and Slovak scientists. Individual showers were monitored by different researchers (Šimek, Porubčan, Hajduk, Štohl). In 1980, Ján Štohl had suggested making extensive observations to monitor the sporadic background in order to assist later corrections of meteor shower data. Staff at the Observatory in Banská Bystrica made the brave decision to not only provide all the observations, but also to carry out basic processing.

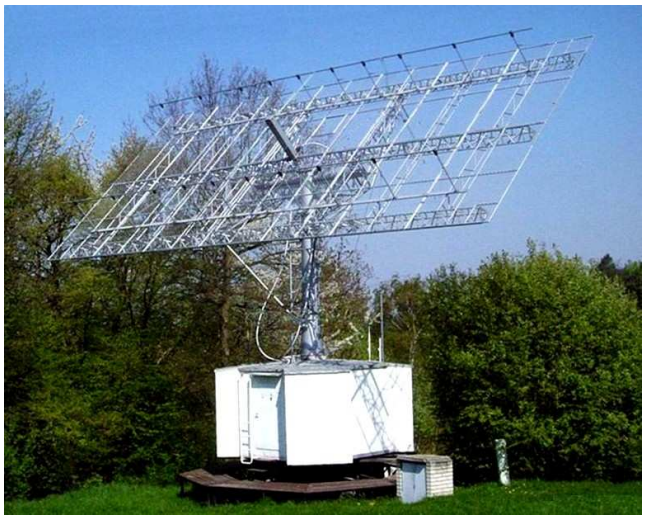

Figure 1 – Meteor radar at Ondřejov.

[1]former worker of Observatory in Banská Bystrica, Slovakia
[2]Email: zimnikoval@gmail.com
[3]Observatory in Žilina, Slovakia
[4]Topographical Institute, Banská Bystrica, Slovakia
[5]Observatory in Banská Bystrica, Slovakia

IMO bibcode WGN-482-zimnikoval-radar
NASA-ADS bibcode 2020JIMO...48...51Z

1.1 Meteor radar at Ondřejov

The radar system was fully rotatable on its vertical axis, thus allowing the selection of the azimuth of the observational area. The aerial was fixed at an elevation of 45°. The antenna beam width between half-power points was 36° in azimuth and 52° in elevation. These values were theoretically derived by Hajduk (1965). The instrument operated at a frequency of 37.5 MHz, with a peak power energy of 25 kW. The pulse width was 10 microseconds, with a repetition frequency of 500 ms. For technical reasons, ranges up to 50 km and from 300 to 350 km were blocked. Radar data was evaluated on an oscilloscope screen, which displayed a vertical line with brighter points corresponding to distance ranges. Echoes were displayed as bright points in the line at appropriate positions between distance markers. The screen was projected by a camera lens on to a continuously moving film. Film speed was 5.6 cm per minute. A 35 mm negative panchromatic cine-film ORWO NP7 was used. Time markers were also projected onto the film, with each 10th second being brighter. The time (hours:minutes) was projected on to the film at each round minute. Amplitudes of meteor echoes were also registered. The radar pulses were sent out every 500 ms and to discriminate real meteor echoes from noise, alternate pulses were made double-strength. The oscilloscope time base covered two pulses in 1 second. If the echo was returned before 500 ms, then the distance was under 300 km and the double-strength echo would appear in the screen zone 350 to 600 km. For a meteor at a distance of more than 350 km, the double-strength echo would appear in the screen zone 50 to 300 km. Thus, a real meteor echo on the film is seen as a point and a check double-strength echo is distanced 300 km from it (Figure 2).

1.2 Method of observation

The observations were divided into four-night blocks for each month during the years 1981 and 1982. A small number of unsuccessful observation blocks were redone during 1983. The dates of the blocks were chosen to coincide with periods of minimal meteor shower activity.

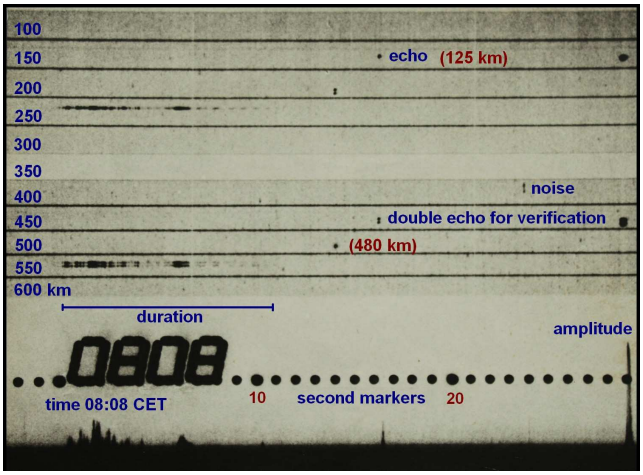

Figure 2 – Part of film record.

Ordinarily, observation started on Monday evening and ended on Friday morning. Most of observations were between 22 hours and 08 hours CET. Observations during the evening hours were excluded so as to avoid strong interference with analogue TV broadcasting at nearby frequencies. On the first night of observation, the aerial was directed to azimuth of the apex. This was achieved by manually moving of all the radar in steps of 3°. On the next night, the radar was directed to the antapex and on the final two nights it was orientated to a fixed azimuth of 0° (North).

1.3 Observational material

All observations were running relatively well. Only the December data was incomplete. There are only the first two nights from December 1981, while in December 1982 all data on the film was wrong. Only four months (January, February, March and April) needed observations in 1983 to complete the data. In total, the observations (successfully recorded on film) covered a time period of about 915 hours and more than 3 kilometres of film records were obtained.

2 Basic processing

Basic processing of the data started in Observatory Banská Bystrica after the few first successful blocks of observations. Film-stored data was displayed on the screen of a special projector called a "documator". The instrument was constructed at our observatory specifically for this work. The data was written on to preprinted paper tables. The table headings were: time data, minute, amplitude, distance and duration of meteor echoes. The process was very slow. About one minute of reduction was required for the evaluation of each 1 minute of film record. Unfortunately, there was no single worker available to carry out this work continuously. All of us had other tasks at the public observatory. Therefore, it took many years to complete the reduction. There was also a second problem. Large amounts of data like ours can only be evaluated using a computer. At that time, there was only a large mainframe machine available. Input data needed to be prepared on magnetic tape or on punched cards. For

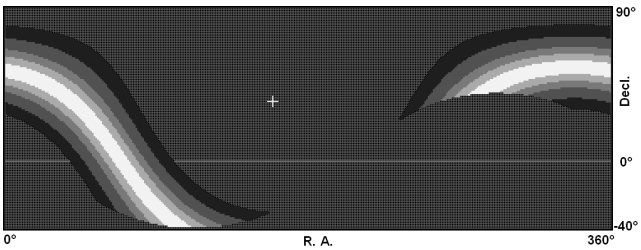

Figure 3 – Working matrix of radiant probability distribution.

this reason, we acquired an old punching machine from the Astronomical Institute in Ondřejov. We started to transfer the data to the card machine, but after making a few cards the instrument broke. We could not find a service that was able to repair it. In 1988, we obtained our first personal computer, a PP 06 (Czechoslovak version of IBM PC), and we started to input data in digital format. Almost half of the whole volume of echoes was digitalized in this way. This data was used for the processing described in this paper.

3 Unsuccessful end of radar observations

After 1989, our society was transformed. Inflation was very high and so the price of film materials rapidly increased. The staff involved with radar work started to develop a digital system for the registration of meteor echoes. A major redesign of radar work was needed and a suitable medium for storing full data had to be found. Modern technology enabled direct measurement of antenna characteristics and it showed that the theoretical antenna beam is partly different from Hajduk's theoretical model. In 1993, Czechoslovakia was divided into two states. In the same year, Ján Štohl, the main person interested in the data, suddenly died. It seemed that the observations were not required anymore. Moreover, given that the data was 10 years old, it was not suitable for reducing the latest shower data.

4 Contemporary processing

The radar data remained stored in digital form on the computers at observatory Banská Bystrica for some 30 years. It consisted of about 60 000 meteor echoes observed during the period from January to September 1981. To complete the data of the year 1981, the final 3 months of observations were transcribed from paper form to digital during 2020. A data set of about 73 000 meteor echoes was obtained.

I have attempted to evaluate the data set using a modern computer. Radar data are generally very poor. For the meteor that caused an echo, its precise time is known, as is a relatively good value of distance from the radar, here measured with an accuracy of 5 km. Other parameters (amplitude and duration) were not included in the processing. The process is based on a fundamental radar model which assumes that the meteor train that returned the transmitted signal back to the antenna must be perpendicular to the aerial axis. Thus, the radiant of the meteor must be at an angular

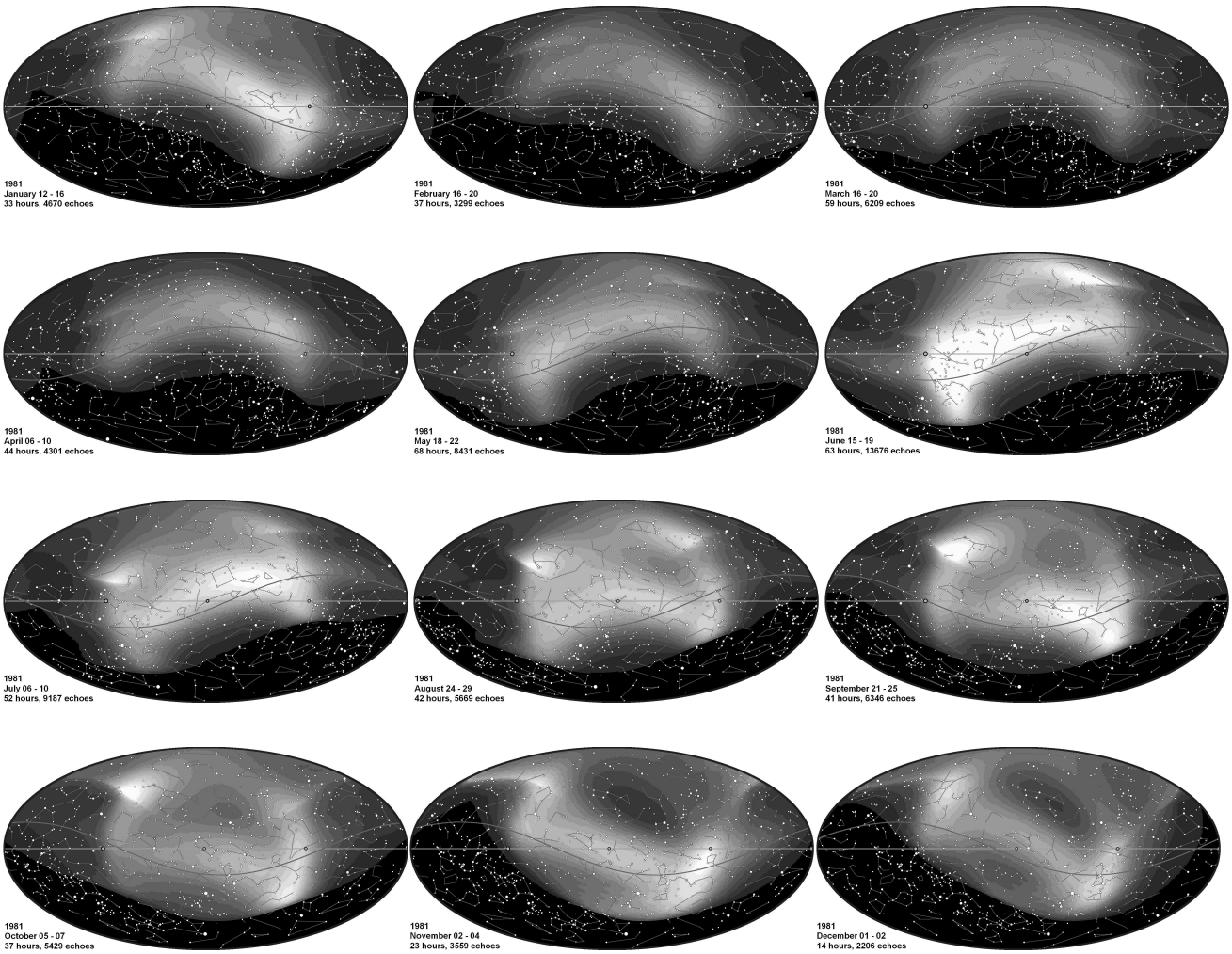

Figure 4 – Radiant distribution on the sky in single months in course of year 1981.

distance from the antenna axis point on the sky of 90° and so must lay on the so-called echo's circle. The azimuth of the circle's center is defined by the azimuth of the radar. Given, however, that the antenna beam has a width of more than 36°, the echo's circle will have a corresponding uncertainty in this azimuth of its centre. The elevation of the radar beam was fixed to 45°, with a width of more than 50°. Here, it was possible to use the distance of the train from the radar to refine its elevation. Assuming the mean value of meteoric layer, we may relatively precisely determine the elevation above horizon of train as center of echo's circle. The value was assumed to be 100 km. Of course, the layer extends from 80 km to 120 km and beyond. This fact is quite well covered given that the probable width of echo's circle would be stretched in elevation like it is in azimuth.

A computer memory field was created – a matrix of 360×130 elements for probable positions of radiants covering the whole sky visible at latitude 50°, with a resolution of 1 degree. The field uses equatorial coordinates. For each element of the field, the angular distance from the most probable center of the echo's circle was calculated. The matrix elements (sky coordinates) with the highest probability of the radiant location (angular distance 86° to 94°) were assigned a value of 5, the area $(82° - 98°)$ was assigned value of 4, the value 3 was assigned for $78° - 102°$, the value 2 for $72° - 108°$ and those up to ± 26 degrees $(64° - 116°)$ were assigned the value 1. Elements farther away do not get a count. This was done for each meteor echo and accumulated for the whole period of interest. These groupings roughly represent the distribution of energy in the radar beam, so are effectively probability levels for individual radiants. A visualization representation of the groupings for one echo is presented in Figure 3. White areas correspond to a value of 5, black areas to values of 1. The white cross marks the most probable position of the train that returned the echo. Parts of an echo's circle that lie below the horizon are not counted in the distribution of probable radiants.

For other data extracts, the values can be summarized in a similar way. Summary probabilities will accumulate around the real positions of sources on the sky. The method is similar to the intersection method for the determination of the radiant from visual observations of a shower.

Data for radiant probabilities were summarized for each block of observation in for each month. It was determined for radar orientations in azimuth of apex, antapex and north all together. To allow for the inequalities in the durations of each set of observations, each

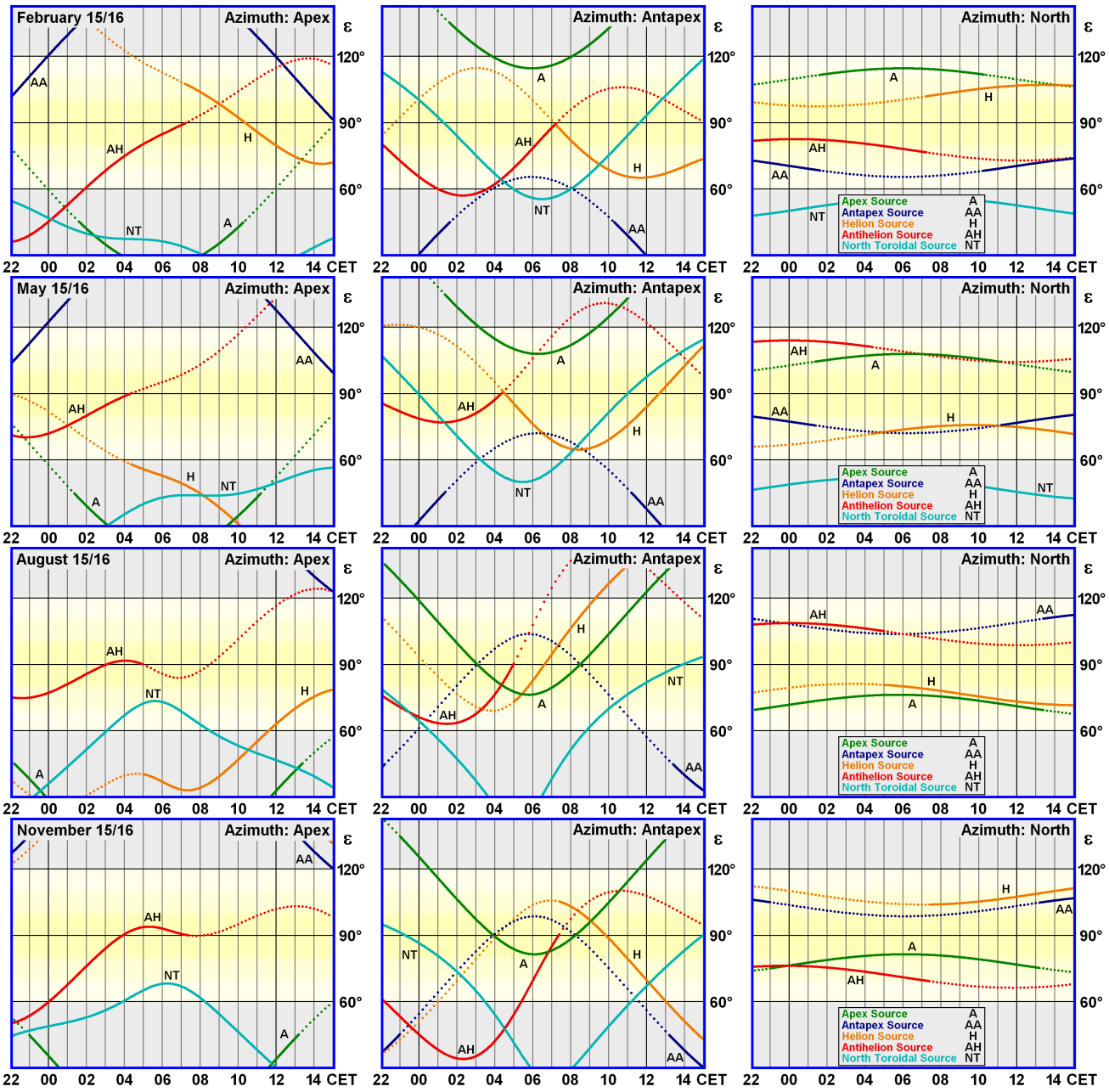

Figure 5 – Detectability of radiants for different azimuth modes of radar.

part (apex, antapex, north) was normalized to value of 10 hours. The data from final matrix could be plotted via a choice of projections (equatorial or the ecliptic coordinate system) on the sky map. The ecliptic coordinate system, with adapted sinusoidal projection centered at the apex, was used. 12 pictures of the sky were generated via this method. Gray scale represent the levels of radiant probabilities. It is not possible to assign absolute values to the scale. A dark gray tint represents minimal activity in the sky, the activity level increases gradually towards the brighter shades of gray, and white is 8 times higher than dark gray. All computed images are shown in Figure 4 (01–12). The central circle is the apex, the left circle on the ecliptic is the Sun and at right is the antihelion. Antapex lies on the left or the right margin of the pictures.

Here we consider the question as to how radar is able to detect single sources of sporadic meteors via the method used. A basic requirement to detect echoes from any source is the necessity of the angular distance being around 90° from the radar axis. Hence, distances of sources from the axis were calculated for all 3 orientation modes of the radar. The diagrams show the elongations of the central parts of single sources. Dotted lines denote that central point of the structure is below the horizon. Only sources that lie around an elongation of 90° (yellow part) may be detected by the radar. Hence, the diagrams show detectability of events during the day in the course of a year (Figures 5). The structures seen on single images of Figure 4 correspond quite well with the diagrams.

There are some asymmetries caused by radar features. According to the antenna diagram, the sensitivity of the radar is near zero for altitudes below 20°. It is not possible to detect radiants around the zenith. Therefore, all figures show a decrease of probabilities

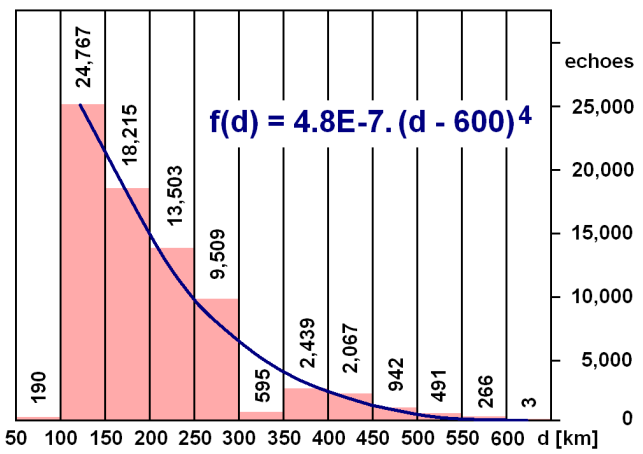

Figure 6 – Distance distribution of echoes from all data in 1981.

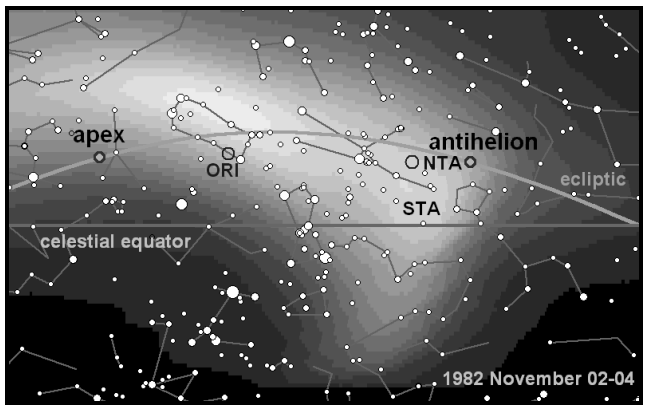

Figure 8 – Possible detection of Southern Taurid activity.

around a declination of 50°. In addition, the observability of echoes near the zenith is also near zero. Thus, few radiants near the horizon can be detected. Almost all figures, however, show extremely high activity near the horizon. It is a fact that the data will contain many more echoes from nearby trains than from more distant ones. In view of this result, a diagram showing the distance distribution of all data was constructed (Figure 6). Values between 300 to 350 km are blocked by technical features of the radar system and no echo may be detected in this range. Echoes apparently from this zone probably result from errors in the reduction process. The diagrams show the other principal attribute of radar observation well. The level of returned signal decreases by the fourth power of the distance. The sensitivity of radar also has the same characteristic. The observed distance distribution corresponds very well with the bi-quadratic function. Coefficients were roughly derived from values in single distance classes. As a result, nearly all echoes are detected at high altitudes (assuming meteoric layer is around 100 km above the Earth' surface) and this leads to higher probability rates near the horizon.

An attempt was made to normalize radiant's probabilities by this factor. The value of the probability distribution for single echoes was multiplied by factor derived from bi-quadratic function with parameters as is given on Figure 6. It was normalized to distance of 250 km. Using this method, a further 12 images were generated. These pictures show the concentrations of probable radiants around the known sporadic meteor sources better. The image for the June observations is shown in Figure 7. It raises the question, however, as to what scientific value can be derived from the distributions after such high corrections. The strong slope of bi-quadratic function leads to large correction values. For an echo with distance of 100 km, the contribution to the whole distribution is normalized by factor of 0.026, whereas for an echo with distance of 600 km this factor is about 33.

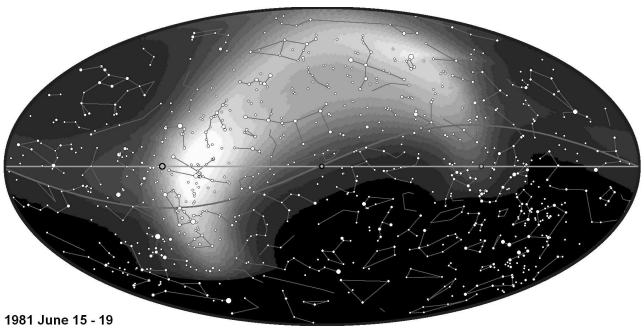

Figure 7 – Image of June observation after correction for influence of distances.

Radiants of meteor showers in principle are also detectable via this method. As was mentioned earlier, observations were targeted towards to periods away from major shower activity. Nevertheless, some showers were active during the observations. These were the η Aquarids in May and the Draconids in October. There was no activity from these showers visible in the results. Only on the November image is there an active region at the position of the radiant of the Southern Taurids (Figure 8). It is not clear, however, whether it is a real effect from this meteor shower. During the same time period, the Northern Taurids and late Orionids were also active and no increase of radiant density was visible from their corresponding regions.

5 Discussion

The presented figures show the distribution of radiants in single periods quite well, but measured data are influenced by many factors. The hours of observation in individual months were not always the same. Most of the observations were carried out at night in the period from 23^{h} to 08^{h} CET, but during May, June, August and, particularly, September, observations continued till 15^{h} CET. Between $15^{h}00^{m}$ to $22^{h}00^{m}$ there were no observations. Given these circumstances, it was not possible to detect sporadic meteor sources equally and symmetrically. This fact caused some differences between the data of individual months. North-south asymmetry is given by topographic position of radar at Ondřejov. Data for each observation block was normalized to same duration of 30 hours per month (by 10 hours each for apex, antapex and north), but there were further influences. Low power electronic equipment was very modern and good quality. Older power electronics – electron tubes and power supply did not work con-

sistently. They were temperature-dependent and were also sensitive to surrounding interferences. Thus, the sensitivity of the radar shows variability and sometimes there were also equipment failures. These factors were not taken into account in the evaluation.

The assumption of perpendicularity is not quite correct. According to the theory, meteor trains are divided into two categories – overdense and underdense trains. They key criterion here is the linear density of electrons, i.e. the number of free electrons in a 1-meter length of the meteor train. Both categories have a different ability to product echoes. Overdense trains sends back echoes with the assumed geometry, but such trains only represent a relatively small percentage of the data. Underdense trains not only reflect the radar signal, but also diffuse it. Due to this, the returned echo may come from another part of the train and so perpendicularity to the radar axis is not guaranteed. Hajduk's model of the antenna diagram, assumed here, does not fully describe real distribution of power in the radar beam and this may lead to some uncertainty in the results presented here.

The detection of meteor shower radiants using this method also introduces some problems. The relation between radar and visual magnitude is not yet understood. Each method of observation is sensitive to a different part of meteoric phenomenon. Radar observations recognize the ability of a meteoroid to create an ionized train, whereas visual (photographic and video) work is dependent on the production of light radiation. Hence, visual activity and radar data can be different.

The distribution of radiants presented here is for the year 1981, but it is probably not possible to generalize it to other years. The number of echoes is dependent on conditions in ionosphere and is also dependent on influences from solar activity (Šimek & Pecina, 2002) and we were close to Solar maximum during 1981.

There is still the need to convert 60 000 echoes from paper format to a computer file. This would involve about 100 hours of work. Given the age of the observational data, however, it seems that there is little desire to complete and evaluate all of these unique observations.

The main role of this paper has been to, at least partially, satisfy the observers who worked on the project. These people are included as co-authors of this paper. In total, the project involved more than 1400 hours of radar observations. For every hour of successful observation, almost the same amount of time was required for the reduction to paper format. Converting these paper forms to computer files would require another 150 hours. Traveling from Banská Bystrica to Ondřejov and back involved about 550 hours on trains and buses. In addition, there were the anonymous people at the observatory in Ondřejov who developed photographic materials. Hence, the unique project required more than 3000 hours of human work.

Acknowledgement

Special thanks are given to Miloš Šimek, scientific worker of Meteor radar at Ondřejov and his technical staff, namely Mr. Holý and Mr. Beránek who helped us to work with radar, provided instruments in good condition and prepared film material for the cameras. We also thank Jozef Gašparec, who covered one block of observations in July 1982.

References

Fabricius J., Kaniansky S., and Škvarka J. (1993). "Observations of sporadic background by the Ondřejov meteor radar". In *Proceedings of the International Meteor Conference, Puimichel, France, 23-26 September 1993*. International Meteor Organization, pages 57–60.

Hajduk A. (1965). "Sensitivity contours of Ondřejov meteor radar". *BAICz*, **16**, 132–135.

Šimek M. and Pecina P. (2002). "Radar sporadic meteor rates and solar activity". *EM&P*, **88**, 115–122.

Handling Editors: Javor Kac and Tracie Heywood

The International Meteor Organization

www.imo.net

Follow us on Facebook InternationalMeteorOrganization

Follow us on Twitter @IMOMeteors

Council

President: Cis Verbeeck,
Bogaertsheide 5, 2560 Kessel, Belgium.
e-mail: cis.verbeeck@scarlet.be

Vice-President: Juraj Tóth,
Fac. Math., Phys. & Inf., Comenius Univ.,
Mlynska dolina, 84248 Bratislava, Slovakia.
e-mail: toth@fmph.uniba.sk

Secretary-General: Robert Lunsford,
14884 Quail Valley Way, El Cajon,
CA 92021-2227, USA. tel. +1 619 755 7791
e-mail: lunro.imo.usa@cox.net

Treasurer: Marc Gyssens, Heerbaan 74,
B-2530 Boechout, Belgium.
e-mail: marc.gyssens@uhasselt.be
BIC: GEBABEBB
IBAN: BE30 0014 7327 5911
Bank transfer costs are always at your expense.

Other Council members:
Javor Kac (see details under WGN)
Detlef Koschny, Zeestraat 46,
NL-2211 XH Noordwijkerhout, Netherlands.
e-mail: detlef.koschny@esa.int
Sirko Molau, Abenstalstraße 13b, D-84072
Seysdorf, Germany. e-mail: sirko@molau.de
Francisco Ocaña Gonzalez, C/ Arquitectura, 7.
28005 Madrid, Spain.
e-mail: francisco.ocana.gonzalez@gmail.com
Vincent Perlerin, 16, rue Georges Bernanos,
51100 Reims, France.
e-mail: vperlerin@gmail.com
Jean-Louis Rault, Société Astronomique de
France, 16, rue de la Vallée, 91360 Epinay sur
Orge, France. e-mail: f6agr@orange.fr
Jürgen Rendtel, Eschenweg 16, D-14476
Marquardt, Germany. e-mail: jrendtel@aip.de

Commission Directors

Visual Commission: Rainer Arlt (rarlt@aip.de)
Generic e-mail address: visual@imo.net
Electronic visual report form:
http://www.imo.net/visual/report/electronic
Video Commission: Sirko Molau (video@imo.net)
Photographic Commission: Bill Ward
(William.Ward@glasgow.ac.uk)
Generic e-mail address: photo@imo.net
Radio Commission: Jean-Louis Rault
(radio@imo.net)
Fireballs: Online fireball reports:
http://fireballs.imo.net

Webmaster

Karl Antier, e-mail: webmaster@imo.net

WGN

Editor-in-chief: Javor Kac
Na Ajdov hrib 24, SI-2310 Slovenska Bistrica,
Slovenia. e-mail: wgn@imo.net;
include METEOR in the e-mail subject line

Editorial board: Ž. Andreić, M. Argo, D.J. Asher,
F. Bettonvil, J. Correira, M. Gyssens,
C. Hergenrother, T. Heywood, J.-L. Rault,
J. Rendtel, C. Verbeeck, S. de Vet, D. Vida.

IMO Sales

Available from the Treasurer or the Electronic Shop on the IMO Website	€	$
IMO membership, including subscription to WGN Vol. 48 (2020)		
Surface mail	26	32
Air Mail (outside Europe only)	49	60
Electronic subscription only	21	25
Proceedings of the International Meteor Conference on paper		
1990, 1991, 1993, 1995, 1996, 1999, 2000, 2002, 2003, per year	9	12
2007, 2010, 2011, per year	15	20
2012, 2013, 2014, 2015 per year	25	34
Proceedings of the Meteor Orbit Determination Workshop 2006	15	20
Radio Meteor School Proceedings 2005	15	20
Handbook for Meteor Observers	15	20
Meteor Shower Workbook	12	16
Electronic media		
Meteor Beliefs Project ZIP archive	6	8

Quadrantids 2020

Composite image of the 84 brightest 2020 Quadrantids, captured using a Sony α7S running at 50 fps at ISO 160.000 with a Sony GM 1.4/24mm lens at F = 1.4. Image Courtesy: Peter C. Slansky.